

# EXTREME-MASS-RATIO BURSTS: PROBES OF MASSIVE BLACK HOLES

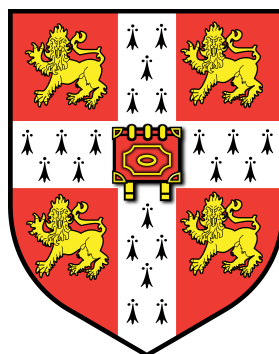
CHRISTOPHER BERRY

Churchill College

and

Institute of Astronomy,  
University of Cambridge

Supervisor: Jonathan Gair



Joint Application Scheme Junior Research Fellowship

15 January 2013

## Abstract

An extreme-mass-ratio burst (EMRB) is a gravitational wave signal emitted when a compact object passes through periapsis on a highly eccentric orbit about a much more massive object, in our case a stellar mass object about a  $10^6 M_\odot$  black hole. EMRBs are an unexplored means of probing the spacetime of massive black holes (MBHs). As a prerequisite for an investigation of the properties of EMRBs and how they could allow us to constrain MBH parameters, it is necessary to construct waveforms. We do so using the computationally efficient numerical kludge approximation. We find that if an EMRB event occurs in the Galaxy, it should be detectable if the periapse distance is  $r_p < 65r_g$  for a  $10M_\odot$  orbiting object, where  $r_g$  is the gravitational radius of the MBH. The signal-to-noise ratio scales approximately as  $\log(\rho) \simeq -2.7\log(r_p/r_g) + \log(\mu/M_\odot) + 4.9$ . To confirm the accuracy of the kludge waveforms we derive an analytic expression for the energy spectrum of gravitational waves from a parabolic Keplerian binary. Comparison with our kludge spectrum shows good agreement.

This work includes sections from

Berry, C.P.L. & Gair, J.R.; Observing the Galaxy's massive black hole with gravitational wave bursts; *Monthly Notices of the Royal Astronomical Society*; **429**(1):589–612; February 2013; [arXiv:1210.2778 \[astro-ph.HE\]](https://arxiv.org/abs/1210.2778)

and

Berry, C.P.L. & Gair, J.R.; Gravitational wave energy spectrum of a parabolic encounter; *Physical Review D*; **82**(10):107501(4); November 2010; [arXiv:1010.3865 \[gr-qc\]](https://arxiv.org/abs/1010.3865),

in addition to unpublished material. This constitutes the greater part of my work on EMRBs; the rest is concerned with astrophysical rate estimation, which is too much to include here. My thesis has two strands: how we can use gravity to probe astrophysical systems, and how astrophysical systems can be used to explore gravitation. The study of EMRBs is former part, which shall make up the majority of the content.

## 1 Background and introduction

Many, if not all, galactic nuclei have harboured a massive black hole (MBH) during their evolution (Lynden-Bell & Rees 1971; Soltan 1982; Rees 1984). Observations have shown that there exist well-defined correlations between the MBHs' masses and the properties of their host galaxies, such as bulge luminosity, mass, velocity dispersion and light concentration (Kormendy & Richstone 1995; Magorrian *et al.* 1998; Ferrarese & Merritt 2000; Gebhardt *et al.* 2000; Graham *et al.* 2001; Tremaine *et al.* 2002; Marconi & Hunt 2003; Häring & Rix 2004; Graham 2007; Graham *et al.* 2011). These suggest coeval evolution of the MBH and galaxy (Peng 2007; Jahnke & Macciò 2011), possibly with feedback mechanisms coupling the two (Haiman & Quataert 2004; Volonteri & Natarajan 2009). The MBH and the surrounding spheroidal component share a common history, such that the growth of one can inform us about the growth of the other.

The best opportunity to study MBHs comes from the compact object in our own galactic centre (GC), which is coincident with Sagittarius A\* (Sgr A\*). Through careful monitoring of stars orbiting the GC, this has been identified as an MBH of mass  $M_\bullet = 4.31 \times 10^6 M_\odot$  at a distance of only  $R_0 = 8.33$  kpc (Gillessen *et al.* 2009).

According to the no-hair theorem, any black hole (BH) should be described completely by just its mass  $M_\bullet$  and spin  $a$ , since we expect the charge of an astrophysical BH to be negligible (Israel 1967, 1968; Carter 1971; Hawking 1972; Robinson 1975; Chandrasekhar 1998). The spin parameter  $a$  is related to the BH's angular momentum  $J$  by

$$J = M_\bullet ac; \quad (1)$$

it is often convenient to use the dimensionless spin

$$a_* = \frac{cJ}{GM_\bullet^2}. \quad (2)$$

As we have a good estimate of the mass, to gain a complete description of the MBH we have only to measure its spin; this shall give us insight into its history and role in the evolution of the Galaxy.

The spin of an MBH is determined by several competing processes. An MBH accumulates mass and angular momentum through accretion (Volonteri 2010). Accretion from a gaseous disc shall spin up the MBH, potentially leading to high spin values (Volonteri *et al.* 2005), while a series of randomly orientated accretion events leads to a low spin value: we expect an average value  $|a_*| \sim 0.1\text{--}0.3$  (King & Pringle 2006; King *et al.* 2008). The MBH also grows through mergers (Yu & Tremaine 2002; Malbon *et al.* 2007). Minor mergers with smaller BHs can decrease the spin (Hughes & Blandford 2003; Gammie *et al.* 2004), while a series of major mergers, between similar mass MBHs, would lead to a likely spin of  $|a_*| \sim 0.7$  (Berti & Volonteri 2008; Berti *et al.* 2007; González *et al.* 2007). Measuring the spin of MBHs shall help us understand the relative importance of these processes, and perhaps give a glimpse into their host galaxies' pasts.

Elliptical and spiral galaxies are believed to host MBHs of differing spins because of their different evolutions: we expect MBHs in elliptical galaxies to have on average higher spins than MBHs in spiral galaxies, where random, small accretion episodes have played a more important role (Volonteri *et al.* 2007; Sikora *et al.* 2007).

It has been suggested that the spin of the Galaxy's MBH could be inferred from careful observation of the orbits of stars within a few milliparsecs of the GC (Merritt *et al.* 2010), although this is complicated because of perturbations due to other stars, or from observations of quasi-periodic oscillations in the luminosity of flares believed to originate from material orbiting close to the innermost stable orbits (Genzel *et al.* 2003; Bélanger *et al.* 2006; Trippe *et al.* 2007; Hamaus *et al.* 2009; Kato *et al.* 2010), though there are difficulties in interpreting these results (Psaltis 2008).

The spins of MBHs in active galactic nuclei have been inferred using X-ray observations of Fe K emission lines (Miller 2007; McClintock *et al.* 2011). So far this has been done for a handful

AGN	$a_*$	Study
1H0707-495	$\geq 0.976$	Zoghbi <i>et al.</i> (2010)
Ark 120	$0.74^{+0.19}_{-0.50}$	Nardini <i>et al.</i> (2011)
Fairall 9	$0.60 \pm 0.07$	Schmoll <i>et al.</i> (2009)
	$0.44^{+0.04}_{-0.11}$	Patrick <i>et al.</i> (2011b)
	$0.39^{+0.48}_{-0.30}$	Emmanoulopoulos <i>et al.</i> (2011)
	$0.67^{+0.10}_{-0.11}$	Patrick <i>et al.</i> (2011a)
	$0.52^{+0.19}_{-0.15}$	Lohfink <i>et al.</i> (2012)
MCG-6-30-15	$0.989^{+0.009}_{-0.002}$	Brenneman & Reynolds (2006)
	$0.86^{+0.01}_{-0.02}$	de la Calle Pérez <i>et al.</i> (2010)
	$0.49^{+0.20}_{-0.12}$	Patrick <i>et al.</i> (2011a)
Mrk 79	$0.7 \pm 0.1$	Gallo <i>et al.</i> (2011)
Mrk 335	$0.70^{+0.12}_{-0.01}$	Patrick <i>et al.</i> (2011b)
Mrk 509	$0.78^{+0.03}_{-0.04}$	de la Calle Pérez <i>et al.</i> (2010)
NGC 3783	$\geq 0.88$	Brenneman <i>et al.</i> (2011)
	$< 0.32$	Patrick <i>et al.</i> (2011a)
NGC 4051	$< 0.94$	Patrick <i>et al.</i> (2011a)
NGC 7469	$0.69^{+0.09}_{-0.09}$	Patrick <i>et al.</i> (2011b)
SWIFT J2127.4+5654	$0.6 \pm 0.2$	Miniutti <i>et al.</i> (2009)
	$0.70^{+0.10}_{-0.14}$	Patrick <i>et al.</i> (2011b)

**Table 1:** Measurements of MBH spin from iron emission lines. The scatter in results indicates the complexities of modelling the accretion disc.

of other galaxies' MBHs, as shown in table 1. Estimates for the spin cover a range of values up to the maximal value for an extremal Kerr black hole. Typical values are in the intermediate range of  $a_* \sim 0.7$  with an uncertainty of about 10% on each measurement.

While we can use the spin of other BHs as a prior, to inform us of what we should expect to measure for the spin of the Galaxy's MBH, it is desirable to have an independent observation, a direct measurement.

An exciting means of inferring information about the MBH is through gravitational waves (GWs) emitted when compact objects (COs), such as stellar mass BHs, neutron stars (NSs), white dwarfs (WDs) or low mass main sequence (MS) stars, pass close by (Sathyaprakash & Schutz 2009). A space-borne detector, such as the Laser Interferometer Space Antenna (LISA) or the evolved Laser Interferometer Space Antenna (eLISA), is designed to be able to detect GWs in the frequency range of interest for these encounters (Bender *et al.* 1998; Danzmann & Rüdiger 2003; Jennrich *et al.* 2011; Amaro-Seoane *et al.* 2012). The identification of waves requires a set of accurate waveform templates covering parameter space. Much work has already been done on the waveforms generated when companion objects inspiral towards an MBH (Glampedakis 2005; Barack 2009); as they orbit, the GWs carry away energy and angular momentum, causing the orbit to shrink until eventually the object plunges into the MBH. These systems are typically formed following two-body encounters so the initial orbits are highly eccentric; a burst of radiation is emitted during each periape passage. These are extreme mass-ratio bursts (EMRBs; Rubbo *et al.* 2006). Assuming that the companion is not scattered from its orbit, and does not plunge straight into the MBH, its orbit evolves, becoming more circular, and it shall begin to continuously emit significant gravitational radiation in the LISA/eLISA frequency range. The resulting signals are extreme mass-ratio inspirals (EMRIs; Amaro-Seoane *et al.* 2007).

Studies of these systems have usually focused upon the phase when the orbit is close to plunge and completes a large number of cycles in the detector's frequency band, allowing a high signal-to-noise ratio (SNR) to be accumulated. Here, we investigate high eccentricity orbits. These are the initial bursting orbits from which an EMRI may evolve, and are the consequence of scattering from two body encounters.. The event rate for the detection of such EMRBs with LISA has been estimated to be as high as  $15 \text{ yr}^{-1}$  (Rubbo *et al.* 2006), although this has been subsequently

revised downwards to the order of  $1 \text{ yr}^{-1}$  (Hopman *et al.* 2007). Even if only a single burst is detected during a mission, this is still an exciting possibility since the information carried by the GW should give an unparalleled probe of the structure of spacetime of the GC. Exactly what can be inferred depends upon the orbit, which we investigate here.

We make the simplifying assumption that all these orbits are marginally bound, or parabolic, since highly eccentric orbits appear almost indistinguishable from an appropriate parabolic orbit. Here “parabolic” and “eccentricity” refer to the energy of the geodesic and not to the geometric shape of the orbit.<sup>1</sup> Following such a trajectory an object may make just one pass of the MBH or, if the periapsis distance is small enough, it may complete a number of rotations. Such an orbit is referred to as zoom-whirl (Glampedakis & Kennefick 2002).

In order to compute the gravitational waveform produced in such a case, we integrate the geodesic equations for a parabolic orbit in Kerr spacetime. We assume that the orbiting body is a test particle, such that it does not influence the underlying spacetime, and that the orbital parameters evolve negligibly during the orbit such that they may be held constant. We use this to construct an approximate numerical kludge (NK) waveform (Babak *et al.* 2007).

In the following we investigate the properties of EMRBs as a means of studying MBHs. We begin in section 2 with the construction of the geodesic orbits; these trajectories are used for the NK waveforms as explained in section 3. In section 4 we establish what the LISA detectors would measure and how the signal would be analysed. This may be skipped with impunity by those familiar with the subject. In section 5 we look at our NK waveforms. We give fiducial power-law fits for SNR as a function of periapse radius, useful for back-of-the-envelope estimates. We confirm the accuracy of the kludge waveforms in section 6 by comparing the energy flux to fluxes calculated using other approaches. The typical error introduced by the NK approximation may be a few percent, but this worsens as the periapsis approaches the last non-plunging orbit. We explain how to extract the information from the bursts in section 7. Results estimating the measurement precision are presented in section 8. The possibility of detecting bursts from extra-galactic sources is studied in section 9, where we find M32 to be promising. Finally, we conclude in section 10 with a summary of our results. EMRBs may be informative if the event rate is high enough for them to be a viable source.

We may proceed to use the waveforms for parameter estimation. Using Markov chain Monte Carlo methods, we have computed the accuracy to which an EMRB can constrain the properties of the MBH. We shall not present these results here, but they do show that EMRBs are useful for measuring the properties of the Galaxy’s MBH.

At the time of writing, there is no currently funded mission. However, LISA Pathfinder, a technology demonstration mission, is due for launch at the end of 2014 (Anza *et al.* 2005; Antonucci *et al.* 2012). Hopefully, a full mission shall follow in the subsequent decade. Since there does not exist a definite mission design, we use the classic LISA design for the majority of this work. It is hoped that any future missions shall have comparable sensitivity, and studies using the LISA design are sensible benchmark for comparison.

Throughout this work we adopt a metric with signature  $(+, -, -, -)$ . Greek indices are used to represent spacetime indices  $\mu = \{0, 1, 2, 3\}$  and lowercase Latin indices from the middle of the alphabet are used for spatial indices  $i = \{1, 2, 3\}$ . Uppercase Latin indices from the beginning of the alphabet are used for the output of the two LISA detector-arms  $A = \{\text{I}, \text{II}\}$ , and lowercase Latin indices from the beginning of the alphabet are used for parameter space. Summation over repeated indices is assumed unless explicitly noted otherwise. Geometric units with  $G = c = 1$  are used where noted, but in general factors of  $G$  and  $c$  are retained.

## 2 Parabolic orbits in Kerr spacetime

### 2.1 The metric and geodesic equations

Astrophysical BHs are described by the Kerr metric (Kerr 1963). In standard Boyer-Lindquist coordinates the line element is (Boyer & Lindquist 1967; Hobson, Efstathiou & Lasenby 2006,

---

<sup>1</sup>Marginally bound Keplerian orbits in flat spacetime are parabolic in both senses.

section 13.7)

$$ds^2 = \frac{\varrho^2 \Delta}{\Sigma^2} c^2 dt^2 - \frac{\Sigma \sin^2 \theta}{\varrho^2} (d\phi - \omega dt)^2 - \frac{\varrho^2}{\Delta} dr^2 - \varrho^2 d\theta^2, \quad (3)$$

where we have introduced functions

$$\varrho^2 = r^2 + a^2 \cos^2 \theta, \quad (4a)$$

$$\Delta = r^2 - \frac{2GM_\bullet r}{c^2} + a^2, \quad (4b)$$

$$\Sigma = (r^2 + a^2)^2 - a^2 \Delta \sin^2 \theta, \quad (4c)$$

$$\omega = \frac{2GM_\bullet ar}{c\Sigma}. \quad (4d)$$

For the remainder of this section we use natural units with  $G = c = 1$ .

Geodesics are parametrized by three conserved quantities (aside from the particle's mass  $\mu$ ): energy (per unit mass)  $E$ , specific angular momentum about the symmetry axis (the  $z$ -axis)  $L_z$ , and Carter constant  $Q$  (Carter 1968; Chandrasekhar 1998, section 62). The geodesic equations are

$$\varrho^2 \frac{dt}{d\tau} = a(L_z - aE \sin^2 \theta) + \frac{r^2 + a^2}{\Delta} T, \quad (5a)$$

$$\varrho^2 \frac{dr}{d\tau} = \pm \sqrt{V_r}, \quad (5b)$$

$$\varrho^2 \frac{d\theta}{d\tau} = \pm \sqrt{V_\theta}, \quad (5c)$$

$$\varrho^2 \frac{d\phi}{d\tau} = \frac{L_z}{\sin^2 \theta} - aE + \frac{a}{\Delta} T, \quad (5d)$$

where we have introduced potentials

$$T = E(r^2 + a^2) - aL_z, \quad (6a)$$

$$V_r = T^2 - \Delta \left[ r^2 + (L_z - aE)^2 + Q \right], \quad (6b)$$

$$V_\theta = Q - \cos^2 \theta \left[ a^2 (1 - E^2) + \frac{L_z^2}{\sin^2 \theta} \right], \quad (6c)$$

and  $\tau$  is proper time. The signs of the  $r$  and  $\theta$  equations may be chosen independently.

For a parabolic orbit  $E = 1$ ; the particle is at rest at infinity. This simplifies the geodesic equations. It also allows us to give a simple interpretation for the Carter constant: this is defined as

$$Q = L_\theta^2 + \cos^2 \theta \left[ a^2 (1 - E^2) + \frac{L_z^2}{\sin^2 \theta} \right], \quad (7)$$

where  $L_\theta$  is the (non-conserved) specific angular momentum in the  $\theta$ -direction ( $V_\theta = L_\theta^2$ ). For  $E = 1$  we have

$$Q = L_\theta^2 + \cot^2 \theta L_z^2 = L_\infty^2 - L_z^2; \quad (8)$$

here  $L_\infty$  is the total specific angular momentum at infinity, where the metric is asymptotically flat (de Felice 1980).<sup>2</sup> This is as in Schwarzschild spacetime.

## 2.2 Integration variables and turning points

In integrating the geodesic equations, difficulties can arise because of the presence of turning points, when the sign of the  $r$  or  $\theta$  geodesic equation changes. The radial turning points are at the periapsis  $r_p$  and at infinity. We may locate the periapsis by finding the roots of

$$V_r = 2M_\bullet r^3 - (L_z^2 + Q) r^2 + 2M_\bullet \left[ (L_z - a)^2 + Q \right] r - a^2 Q = 0. \quad (9)$$

---

<sup>2</sup>See Rosquist *et al.* (2009) for a discussion of the interpretation of  $Q$  in the limit  $G \rightarrow 0$ , corresponding to a flat spacetime.

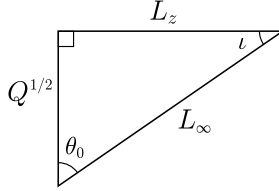


**Figure 1:** The angular momenta  $L_\infty$ ,  $L_z$  and  $\sqrt{Q}$  define a right-angled triangle. The acute angles are  $\theta_0$ , the extremal value of the polar angle, and  $i$ , the orbital inclination (Glampedakis *et al.* 2002).

This has three roots, which we shall denote  $\{r_1, r_2, r_p\}$ ; the periapsis  $r_p$  is the largest real root.<sup>3</sup>

We avoid the difficulties associated with the turning point by introducing angular variables that always increase with proper time (Drasco & Hughes 2004): inspired by Keplerian orbits, we parametrize our trajectory by

$$r = \frac{p}{1 + e \cos \psi}, \quad (10)$$

where  $e = 1$  is the eccentricity and  $p = 2r_p$  is the semilatus rectum. As  $\psi$  covers its range from  $-\pi$  to  $\pi$ ,  $r$  traces out a complete orbit. The geodesic equation for  $\psi$  is

$$\varrho^2 \frac{d\psi}{d\tau} = \left\{ M_* \left[ 2r_p - (r_1 + r_2) (1 + \cos \psi) + \frac{r_1 r_2}{2r_p} (1 + \cos \psi)^2 \right] \right\}^{1/2}. \quad (11)$$

Parametrizing an orbit by its periapsis and eccentricity has the additional benefit of allowing easier comparison with its flat-space equivalent (Gair *et al.* 2005).

The  $\theta$  motion is usually bounded, with  $\theta_0 \leq \theta \leq \pi - \theta_0$ ; in the event that  $L_z = 0$  the particle follows a polar orbit and  $\theta$  covers its full range (Wilkins 1972). The turning points are given by

$$V_\theta = Q - \cot^2 \theta L_z^2 = 0. \quad (12)$$

Changing variable to  $\xi = \cos^2 \theta$ , we have a maximum value  $\xi_0 = \cos^2 \theta_0$  given by

$$\xi_0 = \frac{Q}{Q + L_z^2} = \frac{Q}{L_\infty^2}. \quad (13)$$

See figure 1 for a geometrical visualization. Introducing a second angular variable (Drasco & Hughes 2004)

$$\xi = \xi_0 \cos^2 \chi. \quad (14)$$

Over one  $2\pi$  period of  $\chi$ ,  $\theta$  oscillates from its minimum value to its maximum and back. The geodesic equation for  $\chi$  is

$$\varrho^2 \frac{d\chi}{d\tau} = \sqrt{Q + L_z^2}. \quad (15)$$

### 3 Waveform Construction

We can now calculate the geodesic trajectory. The orbiting body is assumed to follow this track exactly; we ignore evolution due to the radiation of energy and angular momentum, which should be negligible for EMRBs. From this trajectory we calculate the waveform using a semirelativistic approximation (Ruffini & Sasaki 1981): we assume the particle moves along the Kerr geodesic, but radiates as if it were in flat spacetime. This quick-and-dirty technique is known as a numerical kludge (NK), and has been shown to approximate well results computed by more accurate methods (Babak *et al.* 2007). It is often compared to a bead travelling along a wire. The shape of the wire is set by the Kerr geodesic, but the bead moves along in flat space.

<sup>3</sup>We do not find the apoapsis as a (fourth) root to this equation as we have removed it by taking  $E = 1$  before solving. This turning point can be found by setting the unconstrained expression for  $V_r$  equal to zero, and then solving for  $E(r)$ ; taking the limit  $r \rightarrow \infty$  gives  $E \rightarrow 1$  (Wilkins 1972).

### 3.1 Kludge approximation

Numerical kludge approximations aim to encapsulate the main characteristics of a waveform by using the exact particle trajectory (ignoring inaccuracies from radiative effects and from the particle's self-force), whilst saving on computational time by using approximate waveform generation techniques.

We build an equivalent flat-space trajectory by identifying the Boyer-Lindquist coordinates with a set of flat-space coordinates. We consider two choices:

1. Identify the Boyer-Lindquist coordinates with flat-space spherical polars  $\{r_{\text{BL}}, \theta_{\text{BL}}, \phi_{\text{BL}}\} \rightarrow \{r_{\text{sph}}, \theta_{\text{sph}}, \phi_{\text{sph}}\}$ , then define flat-space Cartesian coordinates (Gair *et al.* 2005; Babak *et al.* 2007)

$$\mathbf{x} = \begin{pmatrix} r_{\text{sph}} \sin \theta_{\text{sph}} \cos \phi_{\text{sph}} \\ r_{\text{sph}} \sin \theta_{\text{sph}} \sin \phi_{\text{sph}} \\ r_{\text{sph}} \cos \theta_{\text{sph}} \end{pmatrix}. \quad (16)$$

2. Identify the Boyer-Lindquist coordinates with flat-space oblate-spheroidal coordinates  $\{r_{\text{BL}}, \theta_{\text{BL}}, \phi_{\text{BL}}\} \rightarrow \{r_{\text{ob}}, \theta_{\text{ob}}, \phi_{\text{ob}}\}$  so that the flat-space Cartesian coordinates are

$$\mathbf{x} = \begin{pmatrix} \sqrt{r_{\text{ob}}^2 + a^2} \sin \theta_{\text{ob}} \cos \phi_{\text{ob}} \\ \sqrt{r_{\text{ob}}^2 + a^2} \sin \theta_{\text{ob}} \sin \phi_{\text{ob}} \\ r_{\text{ob}} \cos \theta_{\text{ob}} \end{pmatrix}. \quad (17)$$

These are appealing because in the limit that  $G \rightarrow 0$ , where the gravitating mass goes to zero, the Kerr metric in Boyer-Lindquist coordinates reduces to the Minkowski metric in oblate-spheroidal coordinates.

The two coincide for  $a \rightarrow 0$  or  $r \rightarrow \infty$ .

There is no well motivated argument that either coordinate system must yield an accurate GW; their use is justified *post facto* by comparison with results obtained from more accurate, and computationally intensive, methods (Gair *et al.* 2005; Babak *et al.* 2007). The ambiguity in assigning flat-space coordinates reflects the inconsistency of the semirelativistic approximation: the geodesic trajectory was calculated for the Kerr geometry; by moving to flat spacetime we lose the reason for its existence. This should not be regarded as a major problem; it is an artifact of the basic assumption that the shape of the trajectory is important for determining the character of the radiation, but the curvature of the spacetime in the vicinity of the source is not. By binding the particle to the exact geodesic, we ensure that the waveform has spectral components at the correct frequencies, but by assuming flat spacetime for generation of GWs they shall not have the correct amplitudes.

### 3.2 Quadrupole-octupole formula

Now we have a flat-space particle trajectory  $x_{\text{P}}^{\mu}(\tau)$ , we may apply a flat-space wave generation formula. We use the quadrupole-octupole formula to calculate the gravitational strain (Bekenstein 1973; Press 1977; Yunes *et al.* 2008)

$$h^{jk}(t, \mathbf{x}) = -\frac{2G}{c^6 r} \left( \ddot{I}^{jk} - 2n_i \ddot{S}^{ijk} + n_i \ddot{M}^{ijk} \right)_{t' = t - r/c}, \quad (18)$$

where an over-dot represents differentiation with respect to time  $t$ ,  $t'$  is the retarded time,  $r = |\mathbf{x} - \mathbf{x}_{\text{P}}|$  is the radial distance,  $\mathbf{n}$  is the radial unit vector, and the mass quadrupole  $I^{jk}$ , current quadrupole  $S^{ijk}$  and mass octupole  $M^{ijk}$  are defined by

$$I^{jk}(t') = \int x'^j x'^k T^{00}(t', \mathbf{x}') d^3x'; \quad (19a)$$

$$S^{ijk}(t') = \int x'^j x'^k T^{0i}(t', \mathbf{x}') d^3x'; \quad (19b)$$

$$M^{ijk}(t') = \frac{1}{c} \int x'^i x'^j x'^k T^{00}(t', \mathbf{x}') d^3x', \quad (19c)$$

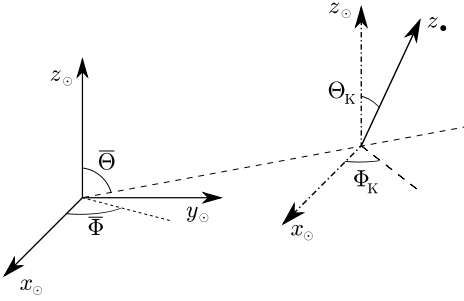


**Figure 2:** The relationship between the MBH's coordinate system  $x_\bullet^i$  and the SS coordinate system  $x_\odot^i$ . The MBH's spin axis is aligned with the  $z_\bullet$ -axis. The orientation of the MBH's  $x$ - and  $y$ -axes is arbitrary. We choose  $x_\bullet$  to be orthogonal to the direction to the SS.

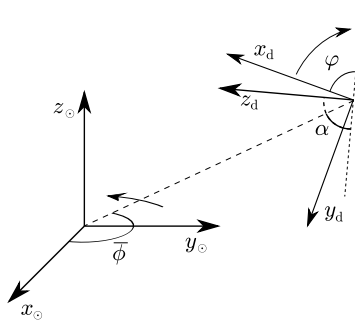


**Figure 3:** The relationship between the detector coordinates  $x_d^i$  and the ecliptic coordinates of the SS  $x_\odot^i$  (Bender *et al.* 1998; Jennrich *et al.* 2011). The detector inclination is  $\alpha = 60^\circ$ .

for energy-momentum tensor  $T^{\mu\nu}$ . This is correct for a slowly moving source. It is the familiar quadrupole formula (Misner *et al.* 1973, section 36.10; Hobson *et al.* 2006, section 17.9), derived from linearized theory, plus the next order terms. For a point mass,  $T^{\mu\nu}$  contains a  $\delta$ -function which allows easy evaluation of the integrals.

Since we are only interested in GWs, we use the transverse-traceless (TT) gauge (Misner *et al.* 1973, box 35.1).

## 4 Signal detection and analysis

### 4.1 The LISA detector

The classic LISA design is a three arm, space-borne laser interferometer (Bender *et al.* 1998; Danzmann & Rüdiger 2003). The arms form an equilateral triangle that rotates as the system's centre of mass follows a circular, heliocentric orbit, trailing  $20^\circ$  behind the Earth. eLISA has a similar design, but has only two arms, which are shorter in length, and trails  $9^\circ$  behind the Earth (Jennrich *et al.* 2011).

To describe the detector configuration, and to transform from the MBH coordinate system to those of the detector, we use three coordinate systems: those of the BH at the GC  $x_\bullet^i$ ; ecliptic coordinates centred at the solar system (SS) barycentre  $x_\odot^i$ , and coordinates that co-rotate with the detector  $x_d^i$ . The MBH's coordinate system and the SS coordinate system are depicted in figure 2. The mission geometry for LISA/eLISA is shown in figure 3. We define the detector coordinates such that the detector-arms lie in the  $x_d$ - $y_d$  plane as in Cutler (1998). We have computed the waveforms in the MBH's coordinates, but it is simplest to describe the measured signal using the detector's coordinates.

The strains measured in the three arms can be combined such that LISA behaves as a pair of  $90^\circ$  interferometers at  $45^\circ$  to each other, with signals scaled by  $\sqrt{3}/2$  (Cutler 1998). We denote the two detectors as I and II and use vector notation  $\mathbf{h}(t) = (h_I(t), h_{II}(t)) = \{h_A(t)\}$  to represent signals from both detectors.

## 4.2 Frequency domain formalism

Having constructed the GW  $\mathbf{h}(t)$  that shall be incident upon the detector, we may consider how to analyse the waveform and extract the information it contains. We briefly recap GW signal analysis, with application to LISA. A more complete discussion can be found in Finn (1992) and Cutler & Flanagan (1994). Adaption for eLISA requires a substitution of the noise distribution, and the removal of the sum over data channels, since it would only have one.

The measured strain  $\mathbf{s}(t)$  is the combination of the signal and the detector noise

$$\mathbf{s}(t) = \mathbf{h}(t) + \mathbf{n}(t); \quad (20)$$

we assume the noise  $\mathbf{n}_A(t)$  is stationary and Gaussian, and that noise in the two detectors is uncorrelated, but shares the same characterisation (Cutler 1998).

The properties of the noise allow us to define a natural inner product and associated distance on the space of signals (Cutler & Flanagan 1994)

$$(\mathbf{g}|\mathbf{k}) = 2 \int_0^\infty \frac{\tilde{g}_A^*(f)\tilde{k}_A(f) + \tilde{g}_A(f)\tilde{k}_A^*(f)}{S_n(f)} df, \quad (21)$$

introducing Fourier transforms

$$\tilde{g}(f) = \mathcal{F}\{g(t)\} = \int_{-\infty}^{\infty} g(t) \exp(2\pi ift) dt, \quad (22)$$

and  $S_n(f)$  is the noise spectral density. The signal-to-noise ratio is approximately

$$\rho[\mathbf{h}] = (\mathbf{h}|\mathbf{h})^{1/2}. \quad (23)$$

The probability of a particular realization of noise  $\mathbf{n}(t) = \mathbf{n}_0(t)$  is

$$p(\mathbf{n}(t) = \mathbf{n}_0(t)) \propto \exp\left[-\frac{1}{2}(\mathbf{n}_0|\mathbf{n}_0)\right]. \quad (24)$$

Thus, if the incident waveform is  $\mathbf{h}(t)$ , the probability of measuring signal  $\mathbf{s}(t)$  is

$$p(\mathbf{s}(t)|\mathbf{h}(t)) \propto \exp\left[-\frac{1}{2}(\mathbf{s} - \mathbf{h}|\mathbf{s} - \mathbf{h})\right]. \quad (25)$$

## 4.3 Noise curve

LISA's noise has two sources: instrumental noise and confusion noise, primarily from WD binaries. The latter may be divided into contributions from galactic and extragalactic binaries. In this work we use the noise model of Barack & Cutler (2004). The shape of the noise curve can be seen in figure 4. The instrumental noise dominates at both high and low frequencies. The confusion noise is important at intermediate frequencies, and is responsible for the cusp around  $10^{-3}$  Hz. eLISA shares the same sources of noise, but is less affected by confusion. Its sensitivity regime is shifted to higher frequencies because of the shorter arm length.

## 4.4 Window functions

There is one remaining complication regarding signal analysis: since we are Fourier transforming a finite signal we encounter spectral leakage; a contribution from large amplitude spectral components leaks into surrounding components (sidelobes), obscuring and distorting the

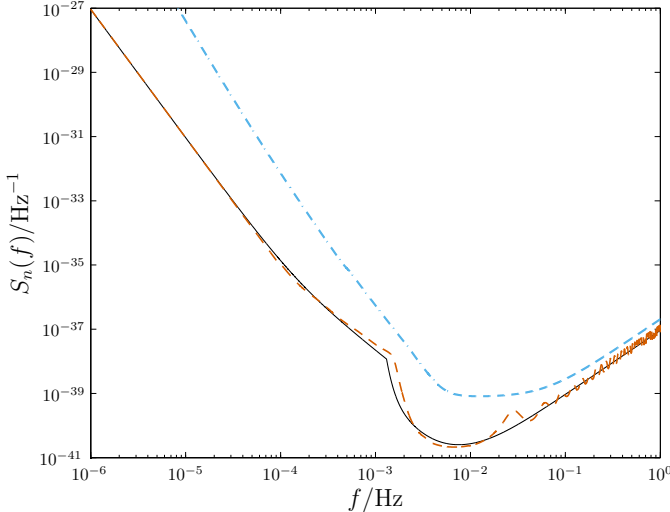


**Figure 4:** The detector noise curves. The solid line indicates the analytic approximation of Barack & Cutler (2004) used in this work. For comparison, the dashed line is from the online LISA sensitivity curve generator (<http://www.srl.caltech.edu/~shane/sensitivity/>; Larson, Hiscock & Hellings 2000; Larson, Hellings & Hiscock 2002). For bursts from the Galactic Centre we are most interested in the low-frequency region where the two curves are the same. The dot-dashed line shows the eLISA noise curve.

spectrum at these frequencies (Harris 1978). This is an inherent problem with finite signals; it shall be as much of a problem when analysing signals from an actual mission as it is computing waveforms here. To mitigate, but unfortunately not eliminate, these effects, the time-domain signal can be multiplied by a window function. We have adopted the Nuttall four-term window with continuous first derivative (Nuttall 1981) for the results presented here.

## 5 Waveforms and detectability

### 5.1 Model parameters

The waveform depends on the properties of the MBH; the CO and its orbit, and the detector.

We assume the position of the detector is known. This is specified by  $\bar{\phi}$  and  $\varphi$ . We chose the initial position so  $\bar{\phi} = 0$  when  $\varphi = 0$  (Cutler 1998); this does not qualitatively influence our results.

We also treat the sky position of the MBH, given by  $\bar{\Theta}$  and  $\bar{\Phi}$ , as known. These are taken as the coordinates of Sgr A\*, as the radio source is expected to be within  $20r_g$  of the MBH (Reid *et al.* 2003; Doeleman *et al.* 2008). We use the J2000.0 coordinates (Reid *et al.* 1999; Yusef-Zadeh *et al.* 1999). These change with time due to the rotation of the SS about the GC; the proper motion is about 6 mas yr<sup>-1</sup>, mostly in the plane of the galaxy (Reid *et al.* 1999; Backer & Sramek 1999; Reid *et al.* 2003). The position is already determined to high accuracy and an EMRB can only give weak constraints on source position, hence we shall not try to infer it.<sup>4</sup>

For our model, the input parameters left to infer are:

1. The MBH's mass  $M_\bullet$ . This is currently well constrained by the observation of stellar orbits about Sgr A\* (Ghez *et al.* 2008; Gillessen *et al.* 2009), with the best estimate being  $M_\bullet = (4.31 \pm 0.36) \times 10^6 M_\odot$ . This depends upon the galactic centre distance  $R_0$  as  $M_\bullet = (3.95 \pm 0.06|_{\text{stat}} \pm 0.18|_{R_0, \text{stat}} \pm 0.31|_{R_0, \text{sys}}) \times 10^6 M_\odot (R_0/8 \text{ kpc})^{2.19}$ , where the

<sup>4</sup>For comparison, an EMRI, which should be more informative, can only give sky localisation to  $\sim 10^{-3}$  steradians (Barack & Cutler 2004; Huerta & Gair 2009).

errors are statistical, independent of  $R_0$ ; statistical from the determination of  $R_0$ , and systematic from  $R_0$  respectively.

2. The spin parameter  $a_*$ . Naively this could be anywhere in the range  $|a_*| < 1$ ; however it is possible to place an upper bound by contemplating spin-up mechanisms. Considering the torque from radiation emitted by an accretion disc, and swallowed by a BH, it can be shown that  $|a_*| \lesssim 0.998$  (Thorne 1974). Magnetohydrodynamical simulations of accretion discs produce a smaller maximum value of  $|a_*| \sim 0.95$  (Gammie *et al.* 2004). The actual spin value could be much lower than this upper bound depending upon the MBH's evolution.

- 3, 4. The orientation angles for the black hole spin  $\Theta_K$  and  $\Phi_K$ .

5. The ratio of the SS-GC distance  $R_0$  and the CO mass  $\mu$ , which we denote as  $\zeta = R_0/\mu$ . This scales the amplitude of the waveform. Bursts, unlike inspirals, do not undergo orbital evolution, hence we cannot break the degeneracy in  $R_0$  and  $\mu$ , and they cannot be inferred separately. The distance, like  $M_\bullet$ , is constrained by stellar orbits, the best estimate being  $R_0 = 8.33 \pm 0.35$  kpc (Gillessen *et al.* 2009). The mass of the orbiting particle depends upon the type of object: whether it is an MS star, WD, NS or BH. Since we shall not know the  $\mu$  precisely, we shall not be able to infer anything more about the distance to the GC.

- 6, 7. The angular momentum of the CO. This can be described using either  $\{L_z, Q\}$  or  $\{L_\infty, \iota\}$ . We employ the latter, as the total angular momentum and inclination are less tightly correlated. Assuming spherical symmetry, we expect  $\cos \iota$  to be uniformly distributed.

- 8–10. A set of coordinates to specify the trajectory. These could be positions at an arbitrary time. We use the angular phases at periape,  $\phi_p$  and  $\chi_p$  (which determines  $\theta_p$ ), as well as the time of periape  $t_p$ .

We are therefore interested in constraining  $d = 10$  parameters.

## 5.2 Waveforms

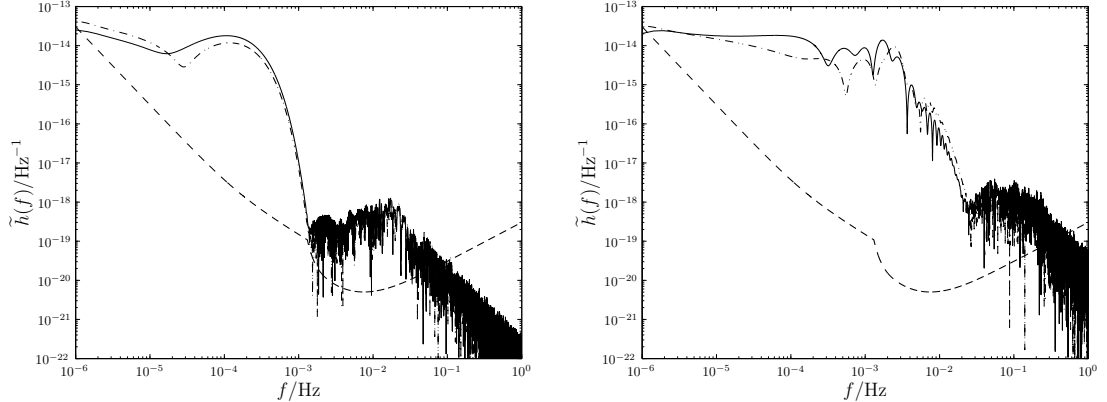
Figure 5 shows example waveforms to demonstrate some of the possible variations in the signal. All these assume the standard mass and position for the MBH as well as a  $\mu = 10M_\odot$  orbiting CO; other (randomly chosen) orbital parameters are specified in the captions. Radii are given in terms of the gravitational radius  $r_g = GM_\bullet/c^2$ .

The plotted waveforms use the spherical polar coordinate system for the NK. Using oblate-spheroidal coordinates makes a small difference: on the scale shown here the only discernible difference would be in figure 5(b); the maximum difference in the waveform (outside the high-frequency tail) is  $\sim 10\%$ . In the other cases the difference is entirely negligible (except in the high-frequency tail, which is not of physical significance). This behaviour is typical; for the closest orbits, with the most extreme spin parameters, the maximum difference in the waveforms may be  $\sim 30\%$ . The difference is largely confined to the higher frequency components, which are most sensitive to the parts of the trajectory closer to the MBH: the change in flat-space radius for the same Boyer-Lindquist radial coordinate causes a slight shift in the shape of the spectrum. Enforcing the same flat-space periape gives worse agreement across the spectrum.

To examine the effect of the coordinate choice, we compare SNRs calculated using the alternative schemes for a selection of orbits. The orbits have periape distances uniformly distributed in log-space between the innermost orbit and  $100r_g$ . Each had a spin and orbital inclination randomly chosen from distributions uniform in  $a_*$  and  $\cos \iota$ .<sup>5</sup> For every periape, five SNRs were calculated, each having a different set of intrinsic parameters specifying the relative orientation of the MBH, the orbital phase and the position of the detector, drawn from

---

<sup>5</sup>The innermost orbit depends upon  $a_*$  and  $\iota$ , hence these are drawn first.



(a) Waveform for  $a_* \simeq 0.12$ ,  $r_p \simeq 15.6r_g$  and  $\iota \simeq 2.1$ . The SNR for the spherical polar kludge waveform (plotted) is  $\rho[\mathbf{h}_{\text{sph}}] \simeq 451$ , for the oblate-spheroidal kludge it is  $\rho[\mathbf{h}_{\text{ob}}] \simeq 451$  (agreement to 0.01%).

(b) Waveform for  $a_* \simeq 0.74$ ,  $r_p \simeq 3.2r_g$  and  $\iota \simeq 1.2$ . The SNR for the spherical polar kludge waveform (plotted) is  $\rho[\mathbf{h}_{\text{sph}}] \simeq 70600$ , for the oblate-spheroidal kludge it is  $\rho[\mathbf{h}_{\text{ob}}] \simeq 74900$ .

**Figure 5:** Example burst waveforms from the galactic centre. The strain  $\tilde{h}_l(f)$  is indicated by the solid line,  $\tilde{h}_{II}(f)$  by the dot-dashed line, and the noise curve by the dashed line. The kludge has been formulated using spherical polar coordinates.

appropriate uniform distributions. We take the mean of  $\ln \rho$  for each set of intrinsic parameters.<sup>6</sup> The MBH parameters were fixed as for the GC.

The ratio of the two SNRs is shown in figure 6. The difference from the coordinate systems is

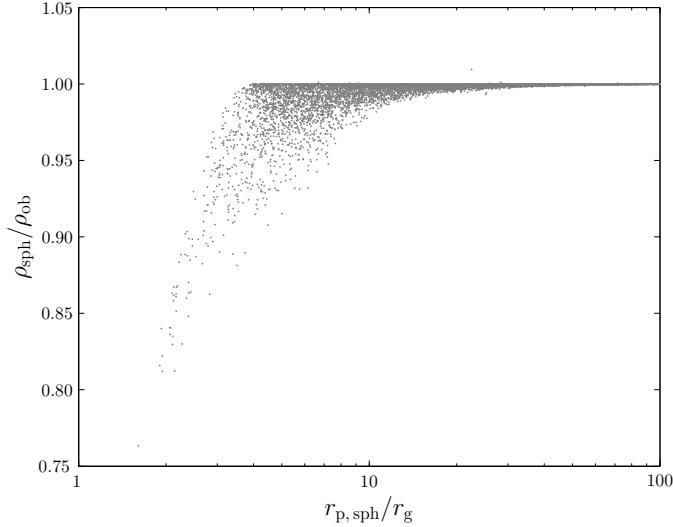


**Figure 6:** Ratio of SNR for a waveform calculated using spherical polar coordinates to that for a waveform using oblate-spheroidal coordinates.

only apparent for orbits with very small periapses. There is agreement to 10% down to  $r_p \simeq 4r_g$ ; the maximal difference may be expected to be  $\sim 20\%$ , this is for periapses that are only obtainable for high spin values.

Since the deviation in the two waveforms is only apparent for small periapses, when the kludge

<sup>6</sup>The logarithm is a better quantity to work with since the SNR is a positive-definite quantity that may be distributed over a range of magnitudes (MacKay 2003, sections 22.1, 23.3). Using median values yields results that are quantitatively similar.

approximation is least applicable, we conclude that the choice of coordinates is unimportant. The potential error of order 10% is no greater than that inherent in the NK approximation (see section 6). Without an accurate waveform template to compare against, we do not know if there is a preferable choice of coordinates. We adopt spherical coordinates for easier comparison with existing work.

### 5.3 Signal-to-noise ratios

The detectability of a burst depends upon its SNR. To characterise the variation of  $\rho$  we calculated SNRs for a range of orbits. These were generated as in section 5.2, we used  $\sim 10^4$  different periapse distances.

The bursts were calculated for a  $1M_\odot$  CO. From equation (18), the amplitude of the waveform is proportional to the CO mass  $\mu$ , and so  $\rho$  is also proportional to  $\mu$ ; a  $10M_\odot$  object would be ten times louder on the same orbit. To make results mass independent, we work in terms of a mass-normalised SNR

$$\hat{\rho}[\mathbf{h}] = \left( \frac{\mu}{M_\odot} \right)^{-1} \rho[\mathbf{h}]. \quad (26)$$

There exists a correlation between the periapse radius and SNR, as shown in figure 7. Closer

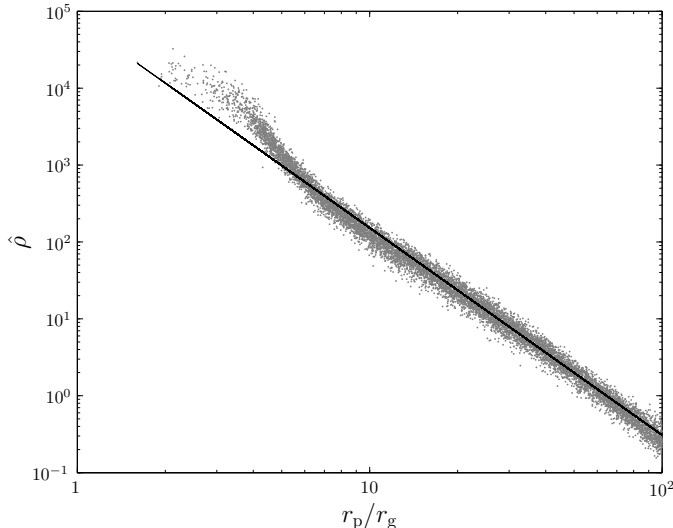


**Figure 7:** Mass-normalised SNR as a function of periapse radius. The plotted points are the values obtained by averaging over each set of intrinsic parameters. The best fit line is  $\log(\hat{\rho}) = -2.69 \log(r_p/r_g) + 4.88$ . This is fitted to orbits with  $r_p > 13.0r_g$  and has a reduced chi-squared value of  $\chi^2/\nu = 1.73$ .

orbits produce louder bursts. To reflect this trend, we have fitted a simple fiducial power law, indicated by the straight line.<sup>7</sup> This was done by maximising the likelihood, assuming  $\ln \rho$  has a Gaussian distribution with standard deviation derived from the scatter because of variation in the intrinsic parameters. The power law is a good fit only for larger periapses. The shape is predominately determined by the noise curve. The change in the trend reflects the transition as from approximately power law behaviour to the bucket of the noise curve. Hence, we fit a power law to orbits with a characteristic frequency of  $f_* = \sqrt{GM_\bullet/r_p} < 1 \times 10^{-3}$  Hz, to avoid spilling into the bucket. Changing the cut-off within a plausible region alters the fit coefficients by around 0.1.<sup>8</sup>

<sup>7</sup>Using oblate-spheroidal coordinates instead of spherical polars gives a fit consistent to within 0.1% as we have excluded the closest orbits.

<sup>8</sup>The power law exponent  $-2.7$  is inconsistent with  $-13/4$  as predicted by the approximate model of Hopman *et al.* (2007). This is the result of their approximate waveform model.

The SNR shows no clear correlation with the other parameters (excluding  $\mu$ ). However, the SNR is sensitive to the intrinsic parameters, in particular the initial position, and may vary by an order of magnitude.

Setting a threshold of  $\rho = 10$ , a  $1M_\odot$  ( $10M_\odot$ ) object would be expected to be detectable if the periapse distance is less than  $27r_g$  ( $65r_g$ ). Hopman *et al.* (2007), assuming a threshold of  $\rho = 5$ , used an approximate form for the SNR based upon the quadrupole component of a circular orbit; their model, with updated parameters for the MBH, predicts bursts would be detectable out to  $66r_g$  ( $135r_g$ ). This is overly optimistic.

## 6 Energy spectra

To check the NK waveforms, we compare the energy spectra calculated from these with those obtained from the classic treatment of Peters & Mathews (1963) and Peters (1964). This calculates GW emission for Keplerian orbits in flat spacetime, assuming only quadrupole radiation. The spectrum produced should be similar to that obtained from the NK in weak fields, that is for large periapses; we do not expect an exact match because of the differing input physics and varying approximations.

In addition to using the energy spectrum, we also use the total energy flux. This contains less information than the spectrum; however, results have been calculated for parabolic orbits in Schwarzschild spacetime using time-domain black hole perturbation theory (Martel 2004). These should be more accurate than results calculated using the Peters and Mathews formalism.

We do not intend to use the kludge waveforms to calculate an accurate energy flux: this would be inconsistent as we assume the orbits do not evolve with time. We only calculate the energy flux as a sanity check, to confirm that the kludge approximation is consistent with other approaches.

### 6.1 Kludge spectrum

A gravitational wave in the TT gauge has an effective energy-momentum tensor (Misner *et al.* 1973, section 35.15)

$$T_{\mu\nu} = \frac{c^4}{32\pi G} \langle \partial_\mu h_{ij} \partial_\nu h^{ij} \rangle, \quad (27)$$

where  $\langle \dots \rangle$  indicates averaging over several wavelengths or periods. The energy flux through a sphere of radius  $R$  is

$$\frac{dE}{dt} = \frac{c^3}{32\pi G} R^2 \int d\Omega \left\langle \frac{dh_{ij}}{dt} \frac{dh^{ij}}{dt} \right\rangle, \quad (28)$$

with  $\int d\Omega$  representing integration over all solid angles. From equation (18) the waves have a  $1/r$  dependence; if we define

$$h_{ij} = \frac{H_{ij}}{r}, \quad (29)$$

we see the flux is independent of  $R$ , as required for energy conservation, and

$$\frac{dE}{dt} = \frac{c^3}{32\pi G} \int d\Omega \left\langle \frac{dH_{ij}}{dt} \frac{dH^{ij}}{dt} \right\rangle. \quad (30)$$

Integrating to find the total energy emitted

$$E = \frac{c^3}{32\pi G} \int d\Omega \int_{-\infty}^{\infty} dt \frac{dH_{ij}}{dt} \frac{dH^{ij}}{dt}. \quad (31)$$

Since we are considering all time, the localization of the energy is no longer of importance and it is unnecessary to average over several periods. Switching to Fourier representation  $\tilde{H}_{ij}(f) = \mathcal{F}\{H_{ij}(t)\}$ ,

$$E = \frac{\pi c^3}{4G} \int d\Omega \int_0^{\infty} df f^2 \tilde{H}^{ij}(f) \tilde{H}_{ij}^*(f), \quad (32)$$

using  $\tilde{H}_{ij}^*(f) = \tilde{H}_{ij}(-f)$  as the signal is real. From this we identify the energy spectrum as

$$\frac{dE}{df} = \frac{\pi c^3}{4G} \int d\Omega f^2 \tilde{H}^{ij}(f) \tilde{H}_{ij}^*(f). \quad (33)$$

## 6.2 Peters and Mathews spectrum

For an orbit of eccentricity  $e$  with periape radius  $r_p$ , Peters & Mathews (1963) give the power radiated into the  $n$ th harmonic of the orbital angular frequency as

$$P(n) = \frac{32}{5} \frac{G^4}{c^5} \frac{M_\bullet^2 \mu^2 (M_\bullet + \mu)(1 - e)^5}{r_p^5} g(n, e), \quad (34)$$

where the function  $g(n, e)$  is defined in terms of Bessel functions of the first kind

$$g(n, e) = \frac{n^4}{32} \left\{ \left[ J_{n-2}(ne) - 2eJ_{n-1}(ne) + \frac{2}{n} J_n(ne) + 2eJ_{n+1}(ne) - J_{n+2}(ne) \right]^2 + (1 - e^2) [J_{n-2}(ne) - 2J_n(ne) + J_{n+2}(ne)]^2 + \frac{4}{3n^2} [J_n(ne)]^2 \right\}. \quad (35)$$

The Keplerian orbital frequency is

$$\omega_1^2 = \frac{G(M_\bullet + \mu)(1 - e)^3}{r_p^3} = (1 - e)^3 \omega_c^2, \quad (36)$$

where  $\omega_c$  is defined as the angular frequency of a circular orbit of radius  $r_p$ . The energy radiated per orbit into the  $n$ th harmonic, that is, at frequency  $\omega_n = n\omega_1$ , is

$$E(n) = \frac{2\pi}{\omega_1} P(n); \quad (37)$$

as  $e \rightarrow 1$  for a parabolic orbit,  $\omega_1 \rightarrow 0$  as the orbital period becomes infinite. The energy radiated per orbit is then the total energy radiated. The spacing of harmonics is  $\Delta\omega = \omega_1$ , giving energy spectrum

$$\frac{dE}{d\omega} \Big|_{\omega_n} \omega_1 = E(n). \quad (38)$$

Changing to linear frequency  $2\pi f = \omega$ ,

$$\frac{dE}{df} \Big|_{f_n} = \frac{128\pi^2}{5} \frac{G^3}{c^5} \frac{M_\bullet^2 \mu^2}{r_p^2} (1 - e)^2 g(n, e) \quad (39)$$

$$= \frac{4\pi^2}{5} \frac{G^3}{c^5} \frac{M_\bullet^2 \mu^2}{r_p^2} \ell(n, e), \quad (40)$$

where the function  $\ell(n, e)$  is defined in the last line. For a parabolic orbit, we must take the limit of  $\ell(n, e)$  as  $e \rightarrow 1$ .

We simplify  $\ell(n, e)$  using the recurrence formulae (Watson 1995, section 2.12)

$$J_{\nu-1}(z) + J_{\nu+1}(z) = \frac{2\nu}{z} J_\nu(z) \quad (41)$$

$$J_{\nu-1}(z) - J_{\nu+1}(z) = 2J'_\nu(z), \quad (42)$$

and eliminate  $n$  using

$$n = \frac{\omega_n}{\omega_1} = (1 - e)^{-3/2} \tilde{f}, \quad (43)$$

where  $\tilde{f} = \omega_n/\omega_c = f_n/f_c$  is a dimensionless frequency. To find the limit we define two new functions

$$A(\tilde{f}) = \lim_{e \rightarrow 1} \left\{ \frac{J_n(ne)}{(1 - e)^{1/2}} \right\}; \quad B(\tilde{f}) = \lim_{e \rightarrow 1} \left\{ \frac{J'_n(ne)}{1 - e} \right\}. \quad (44)$$

To give a well-defined energy spectrum, both of these must be finite.

The Bessel function has an integral representation

$$J_\nu(z) = \frac{1}{\pi} \int_0^\pi \cos(\nu\vartheta - z \sin \vartheta) d\vartheta; \quad (45)$$

we want the limit of this for  $\nu \rightarrow \infty$ ,  $z \rightarrow \infty$ , with  $z \leq \nu$ . Using the stationary phase approximation, the dominant contribution to the integral comes from the regime in which the argument of the cosine is approximately zero (Watson 1995, sections 8.2, 8.43):

$$J_\nu(z) \sim \frac{1}{\pi} \int_0^\pi \cos\left(\nu\vartheta - z\vartheta + \frac{z}{6}\vartheta^3\right) d\vartheta \quad (46)$$

$$\sim \frac{1}{\pi} \int_0^\infty \cos\left(\nu\vartheta - z\vartheta + \frac{z}{6}\vartheta^3\right) d\vartheta; \quad (47)$$

this last expression is an Airy integral and has a standard form (Watson 1995, section 6.4)

$$\int_0^\infty \cos(t^3 + xt) dt = \frac{\sqrt{x}}{3} K_{1/3}\left(\frac{2x^{3/2}}{3^{3/2}}\right), \quad (48)$$

where  $K_\nu(z)$  is a modified Bessel function of the second kind. Using this to evaluate the limit gives

$$J_\nu(z) \sim \frac{1}{\pi} \sqrt{\frac{2(\nu-z)}{3z}} K_{1/3}\left(\frac{2^{3/2}}{3} \sqrt{\frac{(\nu-z)^3}{z}}\right). \quad (49)$$

For our case,

$$J_n(ne) \sim \frac{1}{\pi} \sqrt{\frac{2}{3}} (1-e)^{1/2} K_{1/3}\left(\frac{2^{3/2}\tilde{f}}{3}\right), \quad (50)$$

and the first limiting function is well defined,

$$A(\tilde{f}) = \frac{1}{\pi} \sqrt{\frac{2}{3}} K_{1/3}\left(\frac{2^{3/2}\tilde{f}}{3}\right). \quad (51)$$

To find the derivative we combine equations (42) and (49), and expand to lowest order yielding

$$J'_n(ne) \sim -\frac{1}{2\pi} \sqrt{\frac{2}{3}} (1-e) \left[ 2^{3/2} K'_{1/3}\left(\frac{2^{3/2}\tilde{f}}{3}\right) + \frac{1}{\tilde{f}} K_{1/3}\left(\frac{2^{3/2}\tilde{f}}{3}\right) \right]. \quad (52)$$

We may re-express the derivative using the recurrence formula (Watson 1995, section 3.71)

$$K_{\nu-1}(z) + K_{\nu+1}(z) = -2K'_\nu(z) \quad (53)$$

to give

$$J'_n(ne) \sim \frac{1-e}{\sqrt{3}\pi} \left[ K_{-2/3}\left(\frac{2^{3/2}\tilde{f}}{3}\right) + K_{4/3}\left(\frac{2^{3/2}\tilde{f}}{3}\right) - \frac{1}{\sqrt{2}\tilde{f}} K_{1/3}\left(\frac{2^{3/2}\tilde{f}}{3}\right) \right]. \quad (54)$$

And so finally we obtain the well-defined

$$B(\tilde{f}) = \frac{1}{\sqrt{3}\pi} \left[ K_{-2/3}\left(\frac{2^{3/2}\tilde{f}}{3}\right) + K_{4/3}\left(\frac{2^{3/2}\tilde{f}}{3}\right) - \frac{1}{\sqrt{2}\tilde{f}} K_{1/3}\left(\frac{2^{3/2}\tilde{f}}{3}\right) \right]. \quad (55)$$

Having obtained expressions for  $A(\tilde{f})$  and  $B(\tilde{f})$  in terms of standard functions, we can calculate the energy spectrum for a parabolic orbit. From equation (40)

$$\frac{dE}{df} = \frac{4\pi^2}{5} \frac{G^3}{c^5} \frac{M_\bullet^2 \mu^2}{r_p^2} \ell\left(\frac{f}{f_c}\right), \quad (56)$$

where we have used the limit

$$\ell(\tilde{f}) = [8\tilde{f}^2 B(\tilde{f}) - 2\tilde{f} A(\tilde{f})]^2 + \left(128\tilde{f}^4 + \frac{4\tilde{f}^2}{3}\right) [A(\tilde{f})]^2. \quad (57)$$

This agrees with the  $e = 1$  result of Turner (1977), which was computed by direct integration along unbound orbits. Figure 8 shows how  $\ell(n, e)$  changes with eccentricity including our result for a parabolic encounter. Although more power is radiated into higher harmonics, the peak of the spectrum does not move much: it is always between  $f = f_c$  and  $f = 2f_c$ , with  $f = 2f_c$  for  $e = 0$  and  $f \simeq 1.637f_c$  for  $e = 1$ .

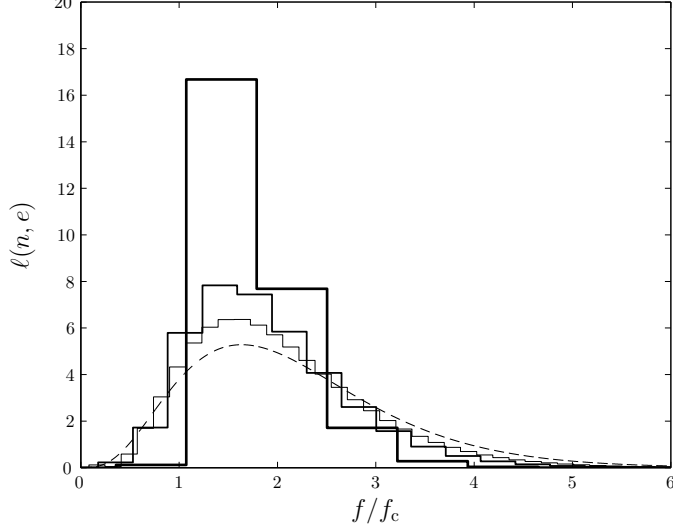


**Figure 8:** The relative energy (per orbit) spectrum  $\ell(n, e)$  for  $e = 0.2$  (heavy line),  $e = 0.5$  (medium line),  $e = 0.7$  (light line), and the limiting result for  $e = 1$  (dashed line) versus frequency. Compare with figure 3 of Peters & Mathews (1963).

### 6.2.1 Total Energy

To check the validity of this limit we can calculate the total energy radiated by integrating equation (56) over all frequencies, or by summing the energy radiated into each harmonic. These must yield the same result. Summing:

$$E_{\text{sum}} = \frac{64\pi}{5} \frac{G^3}{c^5} \frac{M_\bullet^2 \mu^2}{r_p^2} \omega_c (1-e)^{7/2} \sum_n g(n, e), \quad (58)$$

where we have used equations (34), (36) and (37). Peters & Mathews (1963) provide the result

$$\sum_n g(n, e) = \frac{1 + (73/24)e^2 + (37/96)e^4}{(1-e^2)^{7/2}}. \quad (59)$$

Using this,

$$E_{\text{sum}} = \frac{64\pi}{5} \frac{G^3}{c^5} \frac{M_\bullet^2 \mu^2}{r_p^2} \omega_c \frac{1 + (73/24)e^2 + (37/96)e^4}{(1+e)^{7/2}}, \quad (60)$$

which is perfectly well behaved as  $e \rightarrow 1$ ,

$$E_{\text{sum}} = \frac{85\pi}{2^{5/2} 3} \frac{G^3}{c^5} \frac{M_\bullet^2 \mu^2}{r_p^2} \omega_c. \quad (61)$$

Integrating the energy spectrum equation (56) gives

$$E_{\text{int}} = \frac{2\pi}{5} \frac{G^3}{c^5} \frac{M_\bullet^2 \mu^2}{r_p^2} \omega_c \int_0^\infty \ell(\tilde{f}) d\tilde{f}. \quad (62)$$

The integral can be evaluated numerically as

$$\int_0^\infty \ell(\tilde{f}) d\tilde{f} = 12.5216858\dots = \frac{425}{2^{7/2} 3}. \quad (63)$$

The two total energies are consistent,  $E_{\text{int}} = E_{\text{sum}}$ .

### 6.3 Comparison

Two energy spectra are plotted in figure 9 for orbits with periapses of  $r_p = 15.0r_g$ ,  $30.0r_g$  and  $60.0r_g$ . The two spectra appear to be in good agreement, showing the same general shape in the weak-field limit. The NK spectrum is more tightly peaked, but is always within a factor of 2 at the apex. The peak of the spectrum is shifted to a marginally higher frequency in the NK spectrum primarily because of the addition of the current quadrupole and mass octupole terms.

Comparing the total energy fluxes, ratios of the various energies are plotted in figure 10. We introduce an additional energy here, the quadrupole NK energy  $E_{\text{NK(Q)}}$ . This allows easier comparison with the Peters and Mathews energy which includes only quadrupole radiation. It can be calculated in three ways:

1. Inserting the waveform  $\tilde{h}(f)$  generated including only the mass quadrupole term in equation (18) into equation (32) and integrating. This is equivalent to the method used to calculate  $E_{\text{NK}}$ .
2. Numerically integrating the quadrupole GW luminosity (Misner *et al.* 1973, section 36.7; Hobson *et al.* 2006, section 18.7)

$$E = \frac{G}{5c^9} \int \ddot{\mathcal{I}}_{ij} \ddot{\mathcal{F}}^{ij} dt, \quad (64)$$

where  $\mathcal{I}_{ij} = I_{ij} - (1/3)I\delta_{ij}$  is the reduced mass quadrupole tensor. We can obtain this from equation (31), by integrating over all angles when the waveform only contains the mass quadrupole component. This has the advantage of avoiding the effects of spectral leakage or the influence of window functions.

3. Using the analytic expressions for the integral equation (64) given in appendix A of Gair *et al.* (2005).

All three agree to within computational error. No difference is visible on the scale plotted in figure 10. This demonstrates the validity of the code.

We have used the amount of rotation  $\Delta\phi$  as a convenient measure for the abscissa. For an equatorial orbit in Kerr spacetime,

$$\Delta\phi = 2 \int_{r_p}^\infty \frac{d\phi}{dr} dr = \sqrt{\frac{2}{M_\bullet}} L_z \int_{r_p}^\infty \frac{r^2 - 2M_\bullet(1-a/L_z)r}{(r^2 - 2M_\bullet r + a^2)w} dr, \quad (65)$$

where

$$w^2 = r^3 - \frac{L_z^2}{2M_\bullet} r^2 + (L_z - a)^2 r; \quad (66)$$

$L_z$  is the specific angular momentum about the  $z$ -axis;  $a$  is the spin parameter, and we have adopted units with  $G = c = 1$ . We shall find it useful to define

$$r_\pm = M_\bullet \pm \sqrt{M_\bullet^2 - a^2}, \quad (67)$$

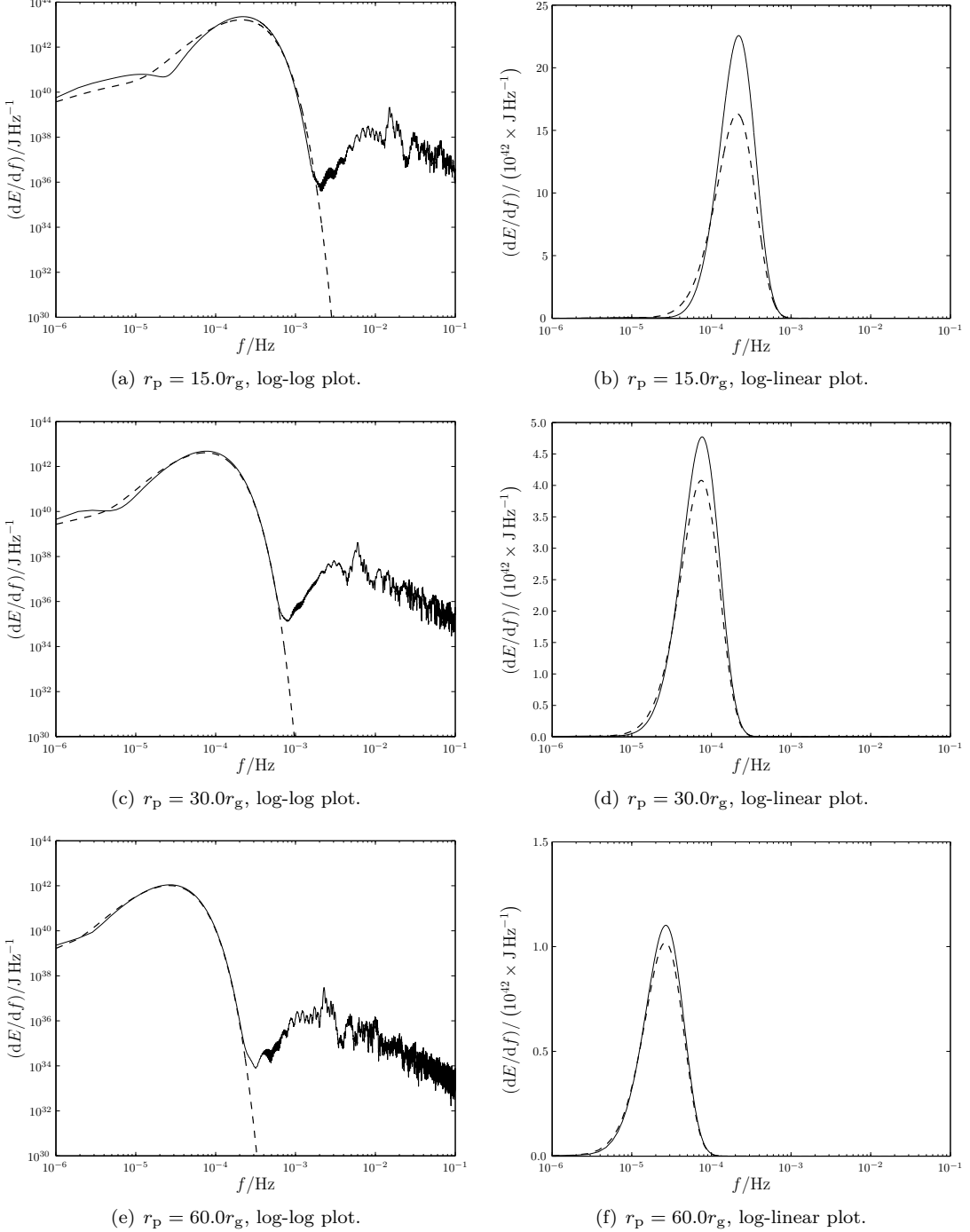


**Figure 9:** Energy spectra for a parabolic orbit of a  $\mu = 10M_\odot$  object about a Schwarzschild BH with  $M_\bullet = 4.31 \times 10^6 M_\odot$ . The spectra calculated from the NK waveform is shown by the solid line and the Peters and Mathews flux is indicated by the dashed line. The NK waveform includes octupole contributions. The high frequency tail is the result of spectral leakage.

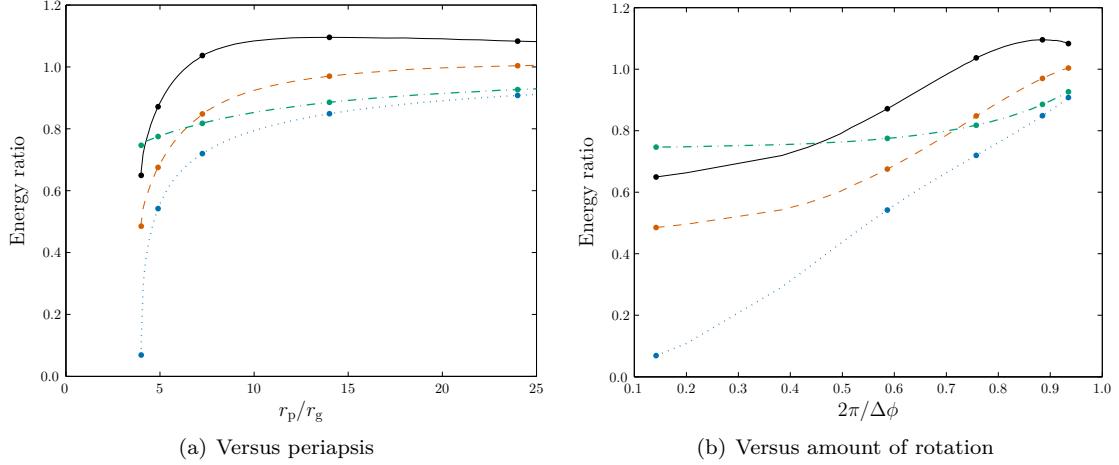


**Figure 10:** Ratios of energies as a function of periapsis  $r_p$  and  $2\pi$  divided by the total angle of rotation in one orbit ( $2\pi/\Delta\phi = 1$  for a Keplerian orbit). The solid line shows the ratio of the numerical kludge and Martel energies  $E_{NK}/E_M$ ; the dashed line shows the ratio of the NK energy calculated using only the mass quadrupole term and the Martel energy  $E_{NK(Q)}/E_M$ ; the dot-dashed line shows the ratio of the quadrupole and quadrupole-octupole NK energies  $E_{NK(Q)}/E_{NK}$ , and the dotted line shows the ratio of the Peters and Mathews and quadrupole NK energies  $E_{PM}/E_{NK(Q)}$ . The spots show the mapping between the two abscissa scales. Compare with figure 4 of Gair *et al.* (2005).

and the two nonzero roots of the cubic  $w^2$

$$r_{p,1} = \frac{L_z^2}{4M_\bullet} \pm \sqrt{\frac{L_z^4}{16M_\bullet^2} - (L_z - a)^2}; \quad (68)$$

the periapsis is the larger root  $r_p > r_1$ . This equation implicitly gives  $L_z$  as a function of  $r_p$ . The integral may be rewritten as

$$\Delta\phi = \sqrt{\frac{2}{M}} L_z \int_{r_p}^{\infty} \frac{1}{w} \left( 1 + \frac{\alpha_+}{r - r_+} + \frac{\alpha_-}{r - r_-} \right) dr, \quad (69)$$

where

$$\alpha_\pm = \pm \frac{2M\alpha_\pm - a^2 L_z}{2L_z \sqrt{M^2 - a^2}}. \quad (70)$$

This may be evaluated using elliptic integrals (Gradshteyn & Ryzhik 2000, 3.131.8, 3.137.8)

$$\Delta\phi = 2L_z \sqrt{\frac{2}{r_p M}} \left[ \frac{\alpha_+}{r_+} \Pi \left( \frac{r_+}{r_p} \middle| \frac{r_1}{r_p} \right) + \frac{\alpha_-}{r_-} \Pi \left( \frac{r_-}{r_p} \middle| \frac{r_1}{r_p} \right) \right], \quad (71)$$

where  $\Pi(n|m) = \int_0^{\pi/2} d\vartheta / (1 - n \sin^2 \vartheta) \sqrt{1 - m \sin^2 \vartheta}$  is the complete elliptic integral of the third kind. In the limit of  $a \rightarrow 0$  we recover the Schwarzschild result (Cutler & Flanagan 1994)

$$\Delta\phi = 2L_z \sqrt{\frac{2}{r_p M}} K \left( \frac{r_1}{r_p} \right), \quad (72)$$

where  $K(m) = \int_0^{\pi/2} d\vartheta / \sqrt{1 - m \sin^2 \vartheta}$  is the complete elliptic integral of the first kind.

The ratios all tend towards one in the weak field, as required, but differences become more pronounced in the strong field. The NK energy is larger than the Peters and Mathews result

$E_{\text{PM}}$ . This behaviour has been seen before for high eccentricity orbits about a non-spinning BH (Gair *et al.* 2005). It may be explained by considering the total path length for the different orbits: the Peters and Mathews spectrum assumes a Keplerian orbit, the orbit in Kerr geometry rotates more than this. The greater path length leads to increased emission of gravitational waves and a larger energy flux. Our bead must travel further along its wire. A good proxy for the path length is the angle of rotation  $\Delta\phi$ ; this is  $2\pi$  for a Keplerian orbit, in Kerr the angle should be  $2\pi$  in the limit of an infinite periapsis, whereas for a periapsis small enough that the orbit shows zoom-whirl behaviour, the total angle may be many times  $2\pi$ . There is a reasonable correlation between the amount of rotation  $2\pi/\Delta\phi$  and the ratio of energies.

Error in the NK energy compared with the time-domain black hole perturbation theory results of Martel comes from two sources: the neglecting of higher order multipole contributions and the ignoring of background curvature. The contribution of the former can be estimated by looking at the difference in the NK energy by including the current quadrupole and mass octupole terms. From figure 10 we see that these terms give a negligible contribution in the weak field, but the difference is  $\sim 20\%$  in the strong field. This explains why the Martel energy  $E_M$  is greater in the strong field, as it includes contributions from all multipoles. Neglecting the background curvature increases the NK energy relative to  $E_M$ . This partially cancels out the error introduced by not including higher order terms: this accidentally leads to  $E_{\text{NK}(Q)}$  being more accurate than  $E_{\text{NK}}$  for  $r_p \gtrsim 10r_g$  (Tanaka *et al.* 1993).

From the level of agreement we may be confident that the NK waveforms are a reasonable approximation. The difference in energy flux is only greater than 10% for very strong fields  $r_p \simeq 4r_g$ ; since this is dependent on the square of the waveform, typical accuracy in the waveform may be  $\sim 5\%$  (Gair *et al.* 2005; Tanaka *et al.* 1993). This is more significant than the variation in waveforms we generally found using the two alternative coordinate systems for the NK (in this case the two coincide because  $a_* = 0$ ).

## 7 Parameter estimation

Having detected a signal, we are interested in what we can learn about the source. We have an inference problem that can be solved by application of Bayes' Theorem (Jaynes 2003, chapter 4): the probability distribution for our parameters given that we have detected the signal  $\mathbf{s}(t)$  is given by the posterior

$$p(\boldsymbol{\lambda}|\mathbf{s}(t)) = \frac{p(\mathbf{s}(t)|\boldsymbol{\lambda})p(\boldsymbol{\lambda})}{p(\mathbf{s}(t))}. \quad (73)$$

Here  $p(\mathbf{s}(t)|\boldsymbol{\lambda})$  is the likelihood of the parameters,  $p(\boldsymbol{\lambda})$  is the prior probability distribution for the parameters, and the evidence  $p(\mathbf{s}(t)) = \int p(\mathbf{s}(t)|\boldsymbol{\lambda}) d^d\lambda$  is, for our purposes, a normalising constant. The likelihood depends upon the realization of noise. If parameters  $\boldsymbol{\lambda}_0$  define a waveform  $\mathbf{h}_0(t) = \mathbf{h}(t; \boldsymbol{\lambda}_0)$ , the probability that we observe signal  $\mathbf{s}(t)$  GW is given by equation (25), so the likelihood is

$$p(\mathbf{s}(t)|\boldsymbol{\lambda}_0) \propto \exp \left[ -\frac{1}{2} (\mathbf{s} - \mathbf{h}_0 | \mathbf{s} - \mathbf{h}_0) \right]. \quad (74)$$

If we were to define this as a probability distribution for the parameters  $\boldsymbol{\lambda}$ , the modal values are the maximum-likelihood (ML) parameters  $\boldsymbol{\lambda}_{\text{ML}}$ . The waveform  $\mathbf{h}(t; \boldsymbol{\lambda}_{\text{ML}})$  is the signal closest to  $\mathbf{s}(t)$ , where distance is defined using the inner product equation (21) (Cutler & Flanagan 1994).

To discover if any parameters can be accurately inferred, we must characterise the form of the posterior. To map out the posterior we employ a Markov chain Monte Carlo (MCMC) approach.

### 7.1 Markov chain Monte Carlo methods

MCMC methods are widely used for inference problems; they are a family of algorithms for integrating over complicated distributions and are efficient for high-dimensional problems (MacKay 2003, chapter 29). Parameter space is explored by constructing a chain of  $N$  samples. The distribution of points visited by the chain maps out the underlying distribution; this becomes

asymptotically exact as  $N \rightarrow \infty$ . Samples are added sequentially, if the current state is  $\boldsymbol{\lambda}_n$  a new point  $\boldsymbol{\lambda}^*$  is drawn and accepted with probability

$$\mathcal{A} = \min \left\{ \frac{\pi(\boldsymbol{\lambda}^*) \mathcal{L}(\boldsymbol{\lambda}^*) \mathcal{Q}(\boldsymbol{\lambda}_n; \boldsymbol{\lambda}^*)}{\pi(\boldsymbol{\lambda}_n) \mathcal{L}(\boldsymbol{\lambda}_n) \mathcal{Q}(\boldsymbol{\lambda}_n; \boldsymbol{\lambda}^*)}, 1 \right\}, \quad (75)$$

setting  $\boldsymbol{\lambda}_{n+1} = \boldsymbol{\lambda}^*$ , where  $\mathcal{L}(\boldsymbol{\lambda})$  is the likelihood, in our case from equation (74);  $\pi(\boldsymbol{\lambda})$  is the prior, and  $\mathcal{Q}$  is a proposal distribution. If the move is not accepted  $\boldsymbol{\lambda}_{n+1} = \boldsymbol{\lambda}_n$ . This is the Metropolis-Hastings algorithm (Metropolis *et al.* 1953; Hastings 1970).

Waiting long enough yields an exact posterior, but it is desirable for the MCMC to converge quickly. This requires a suitable choice for the proposal distribution, which can be difficult, since we do not yet know the shape of the target distribution.

One method to define the proposal is to use the previous results in the chain and refine  $\mathcal{Q}$  by learning from these. Such approaches are known as adaptive methods. Updating using previous points means that the chain is no longer Markovian. Care must be taken to ensure that ergodicity is preserved and convergence obtained (Roberts & Rosenthal 2007; Andrieu & Thoms 2008). To avoid this complication, we follow Haario *et al.* (1999), and use the adapting method as a burn in phase. We have an initial phase where the proposal is updated based upon accepted points. After this we fix the proposal and proceed as for a standard MCMC. By only using samples from the second part, we guarantee that the chain is Markovian and ergodic, whilst still enjoying the benefits of a tailor-made proposal. After only a finite number of samples we cannot assess the optimality of this (Andrieu & Thoms 2008), but the method is still effective.

To tune  $\mathcal{Q}$ , we use an approach based upon the adaptive Metropolis algorithm (Haario *et al.* 2001). The proposal is taken to be a multivariate normal distribution centred upon the current point, the covariance of which is

$$\mathbf{C} = s (\mathbf{V}_n + \varepsilon \mathbf{C}_0), \quad (76)$$

where  $\mathbf{V}_n$  is the covariance of the accepted points  $\{\boldsymbol{\lambda}_1, \dots, \boldsymbol{\lambda}_n\}$ ,  $s$  is a scaling factor that controls the step size,  $\varepsilon$  is a small positive constant (typically 0.0025), and  $\mathbf{C}_0$  is a constant matrix included to ensure ergodicity.

Our adaptation is run in three phases. The initial phase is to get the chain moving. For this  $\mathbf{C}_0^{\text{init}}$  is a diagonal matrix with elements calibrated from initial one dimensional MCMCs. This finishes after  $N_{\text{init}}$  accepted points.

For the second phase, we use the proposal covariance from the initial phase  $\mathbf{C}^{\text{init}}$  for  $\mathbf{C}_0^{\text{main}}$ . We reset the covariance of the accepted points so that it only includes points from this phase. This is the main adaptation phase and lasts until  $N_{\text{main}}$  points have been accepted.

In the final adaptation phase we restart the chain at the true parameter values. We no longer update the shape of the covariance ( $\mathbf{V}_n$  remains fixed), but adjust the step size  $s$  to tune the acceptance rate; it is then fixed, along with everything else, for the final MCMC.

Throughout the adaptation, we update the step size  $s$  after every 100 trial points (whether or not they are accepted). While updating, the covariance  $\mathbf{V}_n$  changes after every 1000 trial points. We set  $N_{\text{init}} = 50000$  and  $N_{\text{main}} = 450000$ .

We initially aimed for an acceptance rate of 0.234; this is optimal for a random walk Metropolis algorithm with some specific high-dimensional target distributions (Roberts *et al.* 1997; Roberts & Rosenthal 2001). In many cases we found better convergence when aiming for a lower acceptance rate, say 0.1. This is not unexpected: the optimal rate may be lower than 0.234 when the parameters are not independent and identically distributed (Bédard 2007, 2008b, a). In practice, the final acceptance rate is (almost always) lower than the target rate as the use of a multivariate Gaussian for the proposal distribution is rarely a good fit at the edges of the posterior. Consequently, the precise choice for the target acceptance rate is unimportant as long as it is of the correct magnitude. Final rates are typically within a factor of 2 of the target value. As an initial choice, we set  $s = 2.38^2/d$ , which is the optimal choice if  $\mathbf{C}$  was the true target covariance for a high dimensional target of independent and identically distributed parameters (Gelman *et al.* 1996; Roberts *et al.* 1997; Roberts & Rosenthal 2001; Haario *et al.* 2001).<sup>9</sup>

<sup>9</sup>Reasonably good results may be obtained by fixing  $s$  at this value, and not adjusting to fine tune the acceptance rate.

To assess the convergence of the MCMC we check the trace plot (the parameters values throughout the run) for proper mixing, that the one and two dimensional posterior plots fill out to a smooth distribution, and that the distribution widths tend towards consistent values.

## 8 Results

### 8.1 Data set

To investigate the information contained in EMRBs, we again considered a range of orbits. The MBH was assumed to have the standard mass and position. The CO was chosen to be  $10M_{\odot}$ , as the most promising candidates for EMRBs would be BHs: they are massive and hence produce higher SNR bursts, they are more likely to be on close orbits as a consequence of mass segregation (Bahcall & Wolf 1977; Alexander & Hopman 2009), and they cannot be tidally disrupted.

Orbits were chosen with periapses uniformly distributed in logarithmic space between the inner-most orbit and  $16r_g$ . The other parameters were chosen randomly from appropriate uniform distributions.

The results of the MCMC runs show strong and complex parameter dependencies. Some example results are shown in figure 11, 12 and 13.

The first is well-behaved. It is almost Gaussian, but we see some asymmetries and imperfections. There are also strong degeneracies, indicated by needle-like distributions. This is a fairly standard example: there are runs which are closer to being Gaussian (especially at higher SNR), and equally there are tighter correlations. The lenticular  $M_{\bullet}$ - $L_{\infty}$  degeneracy is common.

The second shows banana-like degeneracies. These are not uncommon; there are varying degrees of curvature. The more complicated shape makes it harder for the MCMC to converge, so the final distribution is not as smooth as for the first example. The curving degeneracies also bias the one dimensional marginalisations away from the true values.

The third shows more intricate behaviour. This is more rare, but indicates the variety of shapes that is obtainable. Again the convergence is more difficult, so the distributions are rougher around the edges; there is also some biasing due to the curving degeneracies.

These results do not incorporate any priors (save to keep them within realistic ranges); we have not folded in the existing information we have, for example, about the MBH's mass. Therefore, the resulting distributions characterise what we could learn from EMRBs alone. By the time a space-borne GW detector finally flies, we will have much better constraints on some parameters.

It is possible to place good constraints from the closest orbits. These can provide sufficient information to give beautifully behaved posteriors although significant correlation between parameters persists.

### 8.2 Distribution widths

Characteristic distribution widths are shown in figure 14. Plotted are the standard deviation  $\sigma_{SD}$ ; a scaled 50-percentile range  $\sigma_{50} = W_{50}/1.34898$ , where  $W_{50}$  is the range that contains the median 50% of points, and a scaled 95-percentile range  $\sigma_{95} = W_{95}/3.919928$ , where  $W_{95}$  is the 95% range. These widths are equal for a normal distribution. Filled circles are used for runs that appear to have converged. Open circles are for those yet to converge, but which appear to be approaching an equilibrium state; widths should be accurate to within a factor of a few. For guidance, the dotted line corresponds to the current measurement uncertainty for  $M_{\bullet}$ ; the dashed lines are from uniform priors for  $a_*$ ,  $\Phi_K$ ,  $\phi_p$ ,  $\chi_p$ ,  $\cos \Theta_K$  and  $\cos \iota$ , and, for completeness, the solid line indicates the total prior range. We have no expectations for the width of the MBH mass distribution with respect to the current value; however, we would expect that the recovered distributions for the other parameters are narrower than for the case of complete ignorance. This may not be the case if the distribution is multimodal: in this event using the width is an inadequate description of the distribution. Only a few unconverged runs exceed these limits, and some appear to be multimodal.

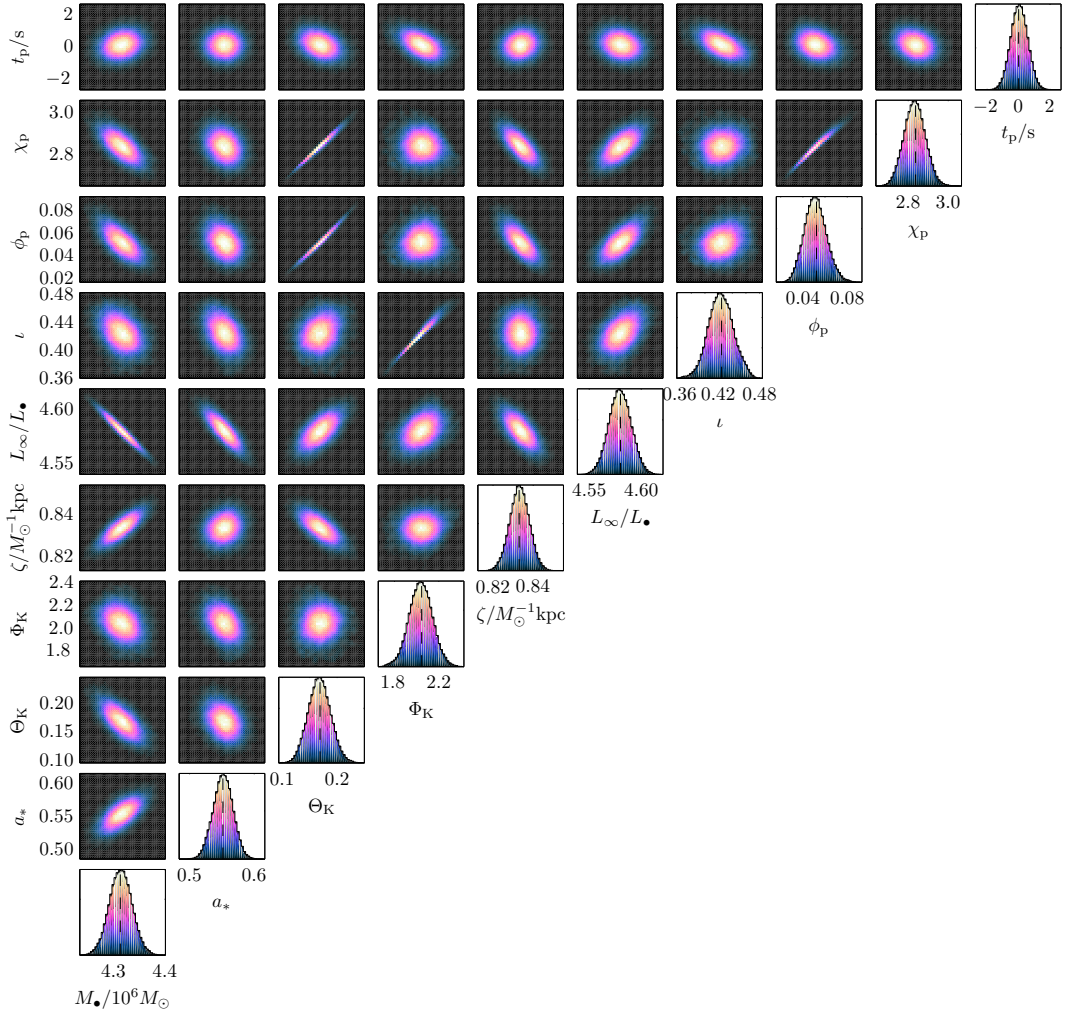


**Figure 11:** Marginalised one and two dimensional posteriors. The scales are identical in both sets of plots. The dotted line indicates the true value. These distributions are fairly cromulent and well converged. Angular momentum is in units of  $L_\bullet = GM_\bullet c^{-1}$ . The input orbit has  $r_p \simeq 8.54r_g$  and  $\rho \simeq 916$ .

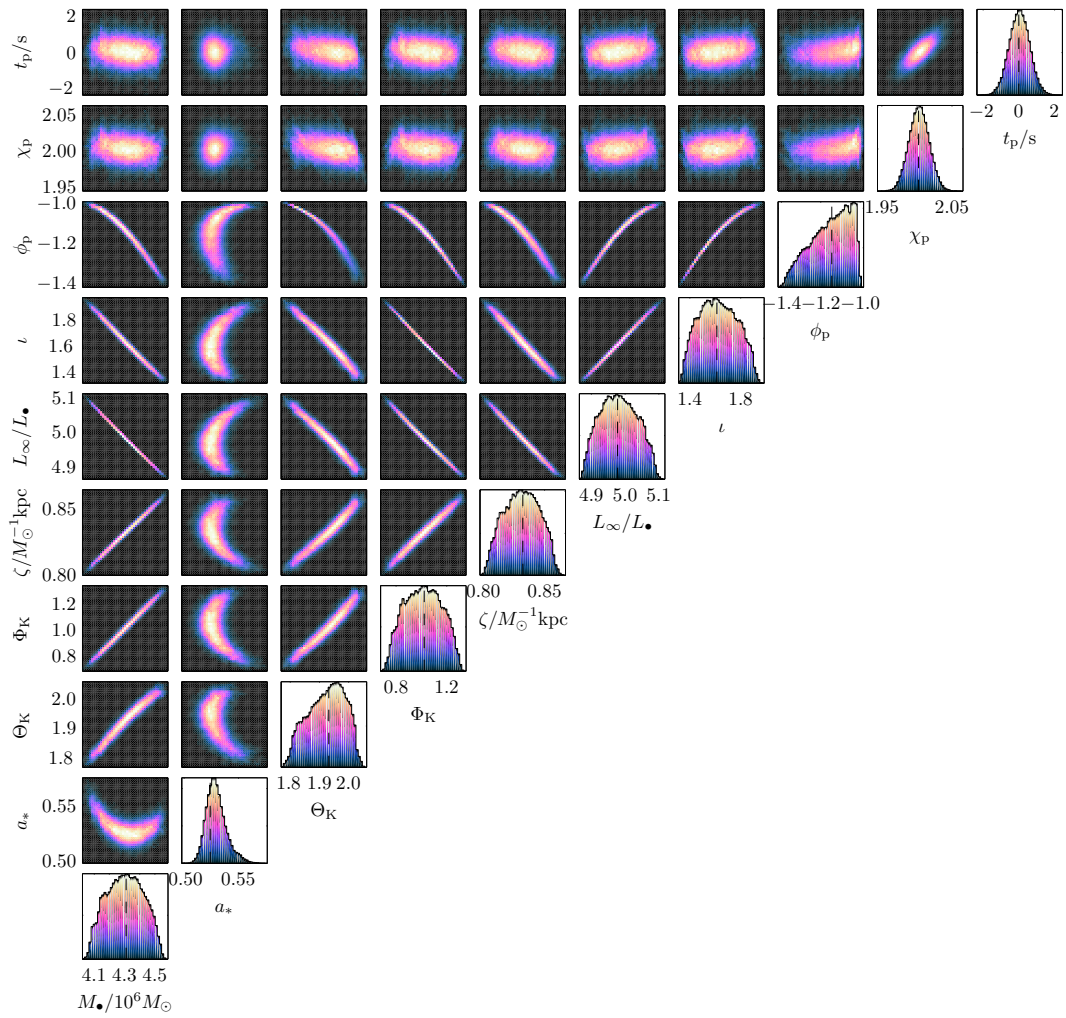


**Figure 12:** Marginalised one and two dimensional posteriors. The scales are identical in both sets of plots. The dotted line indicates the true value. These distributions show definite non-gaussianity. The input orbit has  $r_p \simeq 9.86r_g$  and  $\rho \simeq 1790$ .

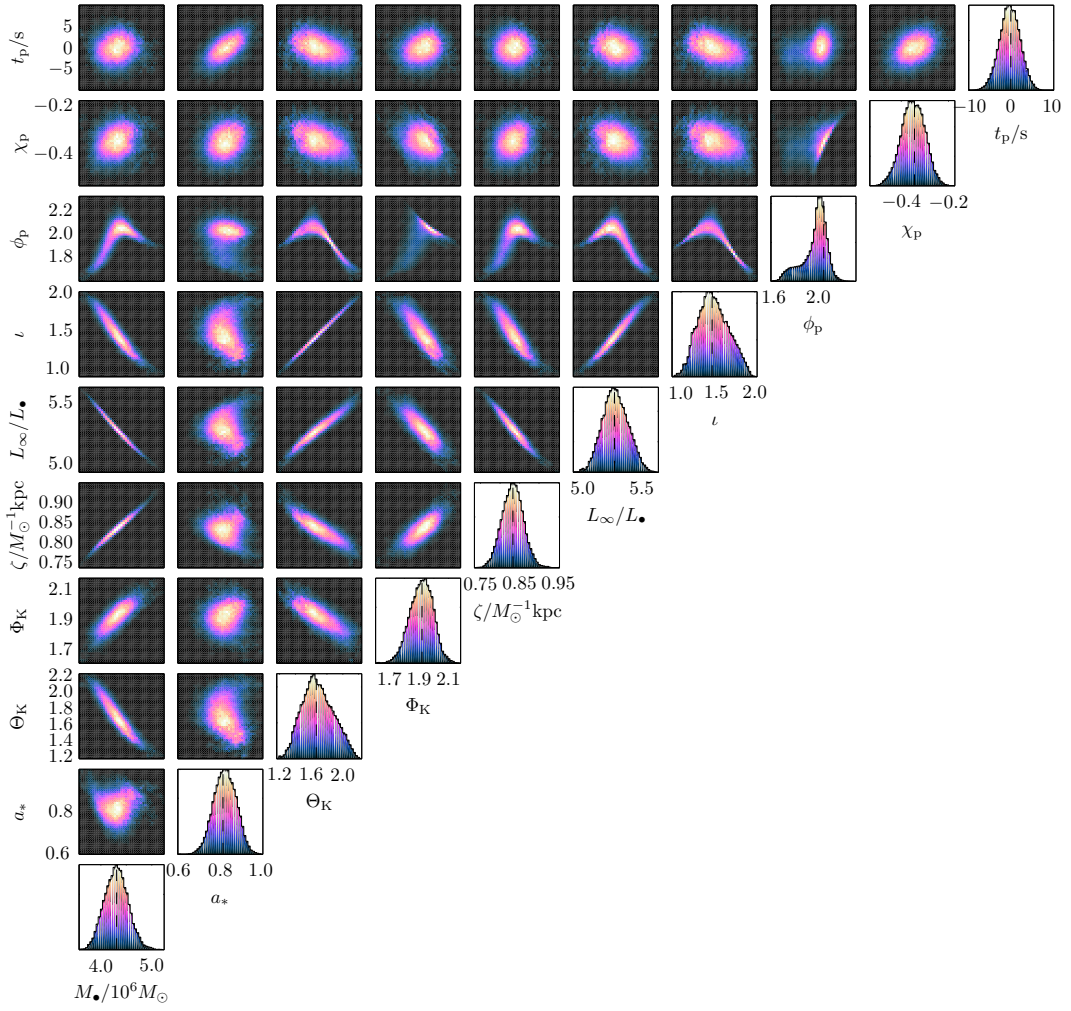


**Figure 13:** Marginalised one and two dimensional posteriors. The scales are identical in both sets of plots. The dotted line indicates the true value. These distributions show complicated degeneracies. The input orbit has  $r_p \simeq 11.60r_g$  and  $\rho \simeq 590$ .

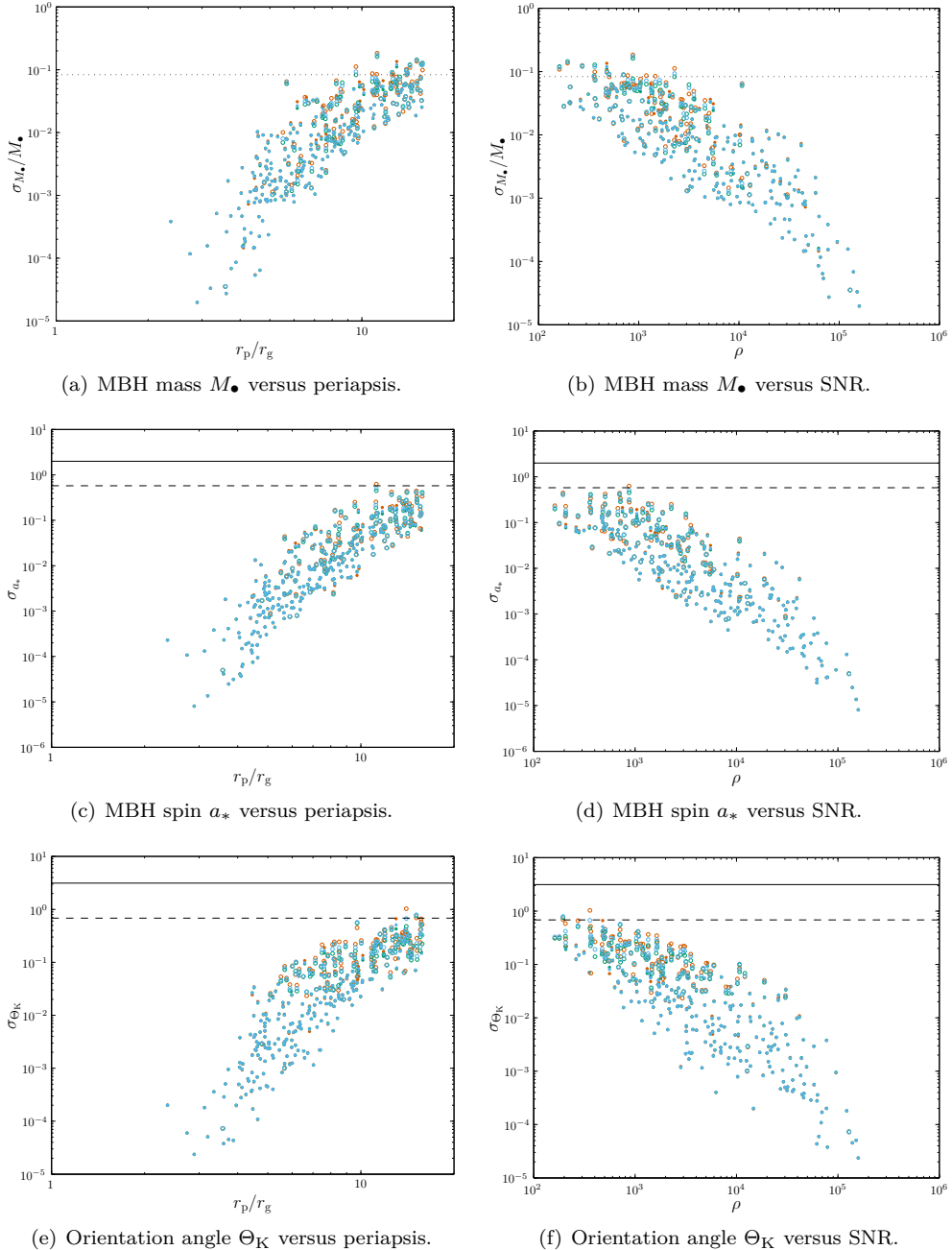


**Figure 14:** Distribution widths as functions of periapse  $r_p$  and SNR  $\rho$ . Light blue is used for the standard deviation, red is the scaled 50-percentile range and green is the scaled 95-percentile range: all three coincide for a normal distribution. Filled circles are used for converged runs, open circles for those yet to converge. The dotted line indicates the current uncertainty for  $M_\bullet$ ; the dashed lines the standard deviation for an uninformative prior, and the solid lines the total prior range.

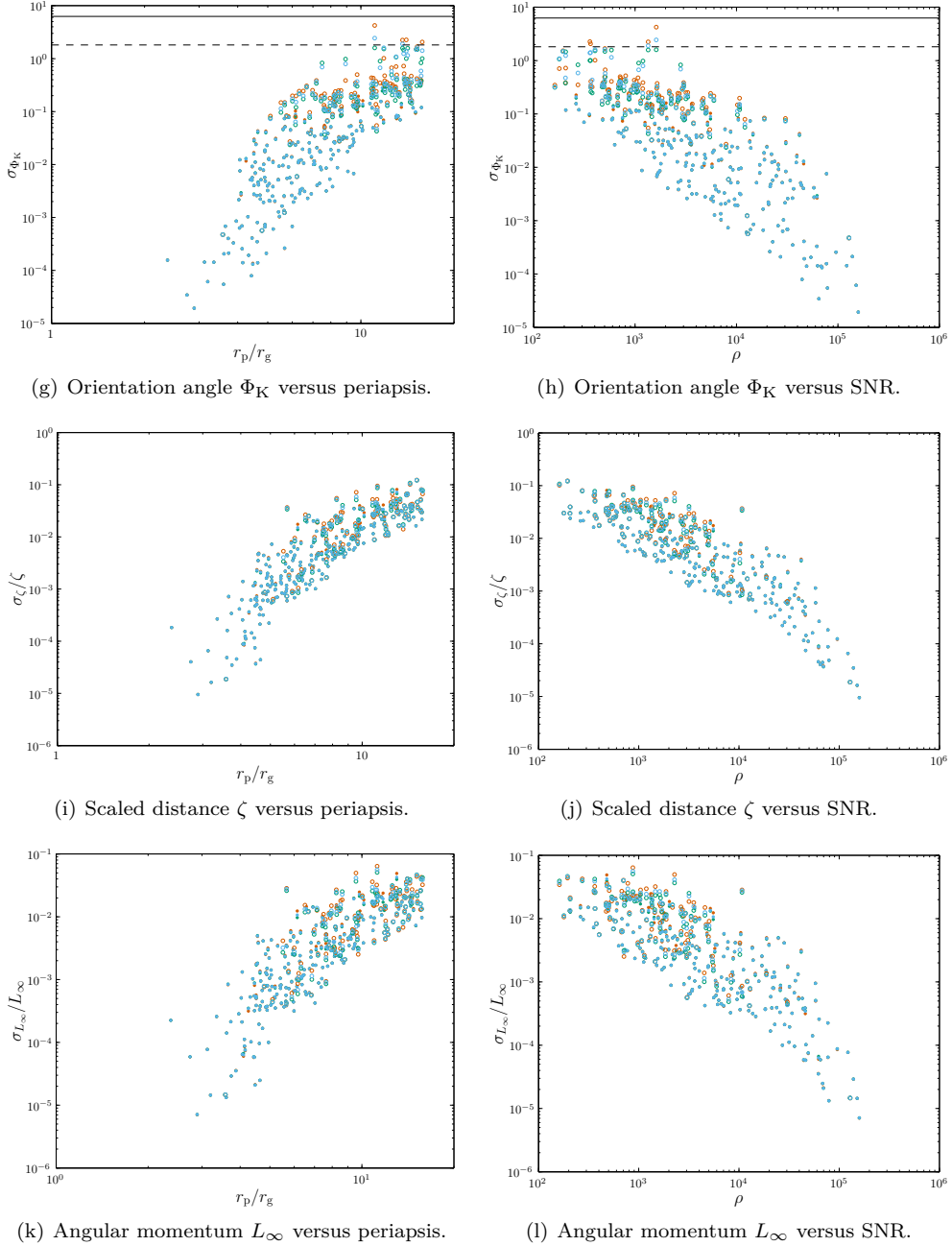


**Figure 14:** Distribution widths as functions of periapse  $r_p$  and SNR  $\rho$ . Light blue is used for the standard deviation, red is the scaled 50-percentile range and green is the scaled 95-percentile range: all three coincide for a normal distribution. Filled circles are used for converged runs, open circles for those yet to converge. The dotted line indicates the current uncertainty for  $M_\bullet$ ; the dashed lines the standard deviation for an uninformative prior, and the solid lines the total prior range.

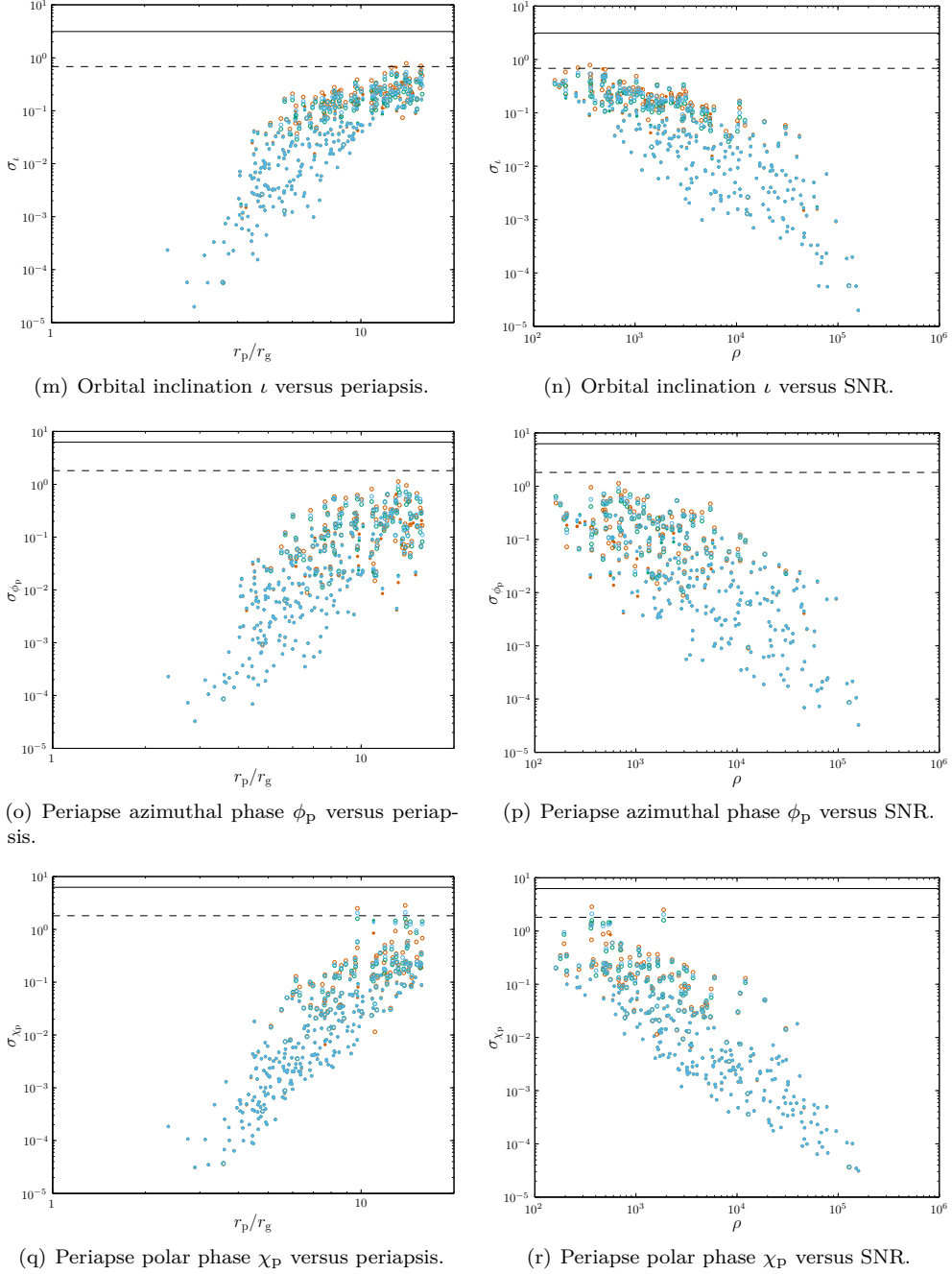


**Figure 14:** Distribution widths as functions of periapse  $r_p$  and SNR  $\rho$ . Light blue is used for the standard deviation, red is the scaled 50-percentile range and green is the scaled 95-percentile range: all three coincide for a normal distribution. Filled circles are used for converged runs, open circles for those yet to converge. The dotted line indicates the current uncertainty for  $M_\bullet$ ; the dashed lines the standard deviation for an uninformative prior, and the solid lines the total prior range.

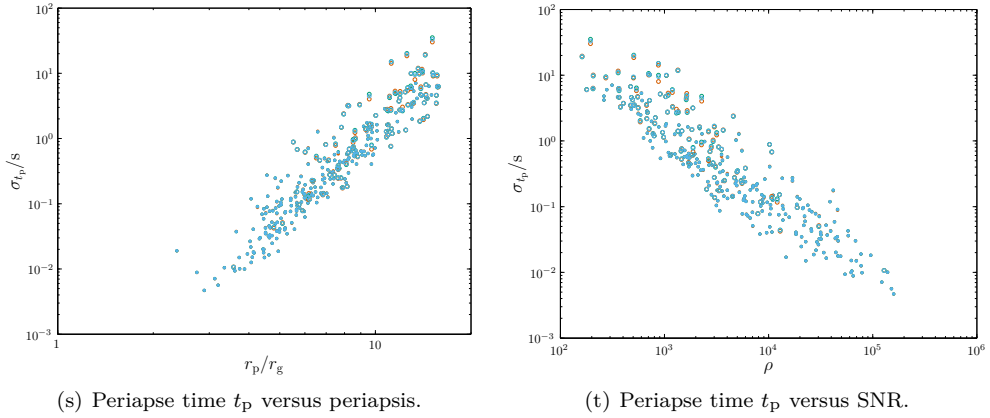


**Figure 14:** Distribution widths as functions of periapsis  $r_p$  and SNR  $\rho$ . Light blue is used for the standard deviation, red is the scaled 50-percentile range and green is the scaled 95-percentile range: all three coincide for a normal distribution. Filled circles are used for converged runs, open circles for those yet to converge. The dotted line indicates the current uncertainty for  $M_\bullet$ ; the dashed lines the standard deviation for an uninformative prior, and the solid line the total prior range.

The widths show a trend of decreasing with decreasing periapsis or increasing SNR, but there is a large degree of scatter. There does not appear to be a strong dependence upon any single input parameter, with the exception of the spin. The widths for  $\iota$ ,  $\Theta_K$ ,  $\Phi_K$ ,  $\phi_p$  and  $\chi_p$  increase for smaller spin magnitudes. The dependence is shown in figure 15. These parameters are defined with reference to the coordinate system established by the spin axis: for  $a_* = 0$  we have spherical symmetry and there would be ambiguity in defining them. Therefore, it makes sense that they can be more accurately determined for larger spin magnitudes. The width for  $a_*$ , however, shows no clear correlation.

### 8.3 Scientific potential

Having quantified the precision with which we could infer parameters from an EMRB waveform, we can now consider if it is possible to learn anything new.

Of paramount interest are the MBH mass and spin. The current uncertainty in the mass is  $\sigma_{M_\bullet} = 0.36 \times 10^6 M_\odot$  ( $\sim 8\%$ ). There are few runs amongst our data set that are not better than this: it appears that orbits of a  $\mu = 10 M_\odot$  CO with periapses  $r_p \lesssim 13r_g$  should be able to match our current observational constraints. However, the EMRB is an independent measurement, and so a measurement of comparable precision to the current bound can still be informative. Accuracy of 1% could be possible if  $r_p \lesssim 8r_g$ .

The spin is less well constrained. To obtain an uncertainty for the magnitude of 0.1, comparable to that achieved in X-ray measurements of active galactic nuclei, it appears that the periapsis needs to be  $r_p \lesssim 11r_g$ . For smaller periapses, the uncertainty can be much less, indicating that an EMRB could be an excellent probe. The orientation angles for the spin axis may be constrained to better than 0.1 for  $r_p \lesssim 11r_g$ . It may well be possible to learn both the direction and the magnitude of the spin. This could illuminate the MBH's formation.

We have no *a priori* knowledge about the CO or its orbit, so anything we learn would be new. However, this is not particularly useful information, unless we observe multiple bursts, and can start to build up statistics for the dynamics of the GC. Using current observations for the distance to the GC, which could be further improved by the mass measurement from the EMRB, it is possible to infer a value for the mass  $\mu$  from  $\zeta$ . This could inform us of the nature of the object (BH, NS or WD) and be a useful consistency check. A small value of  $\zeta$ , indicating a massive CO, would be unambiguous evidence for the existence of a stellar mass black hole.

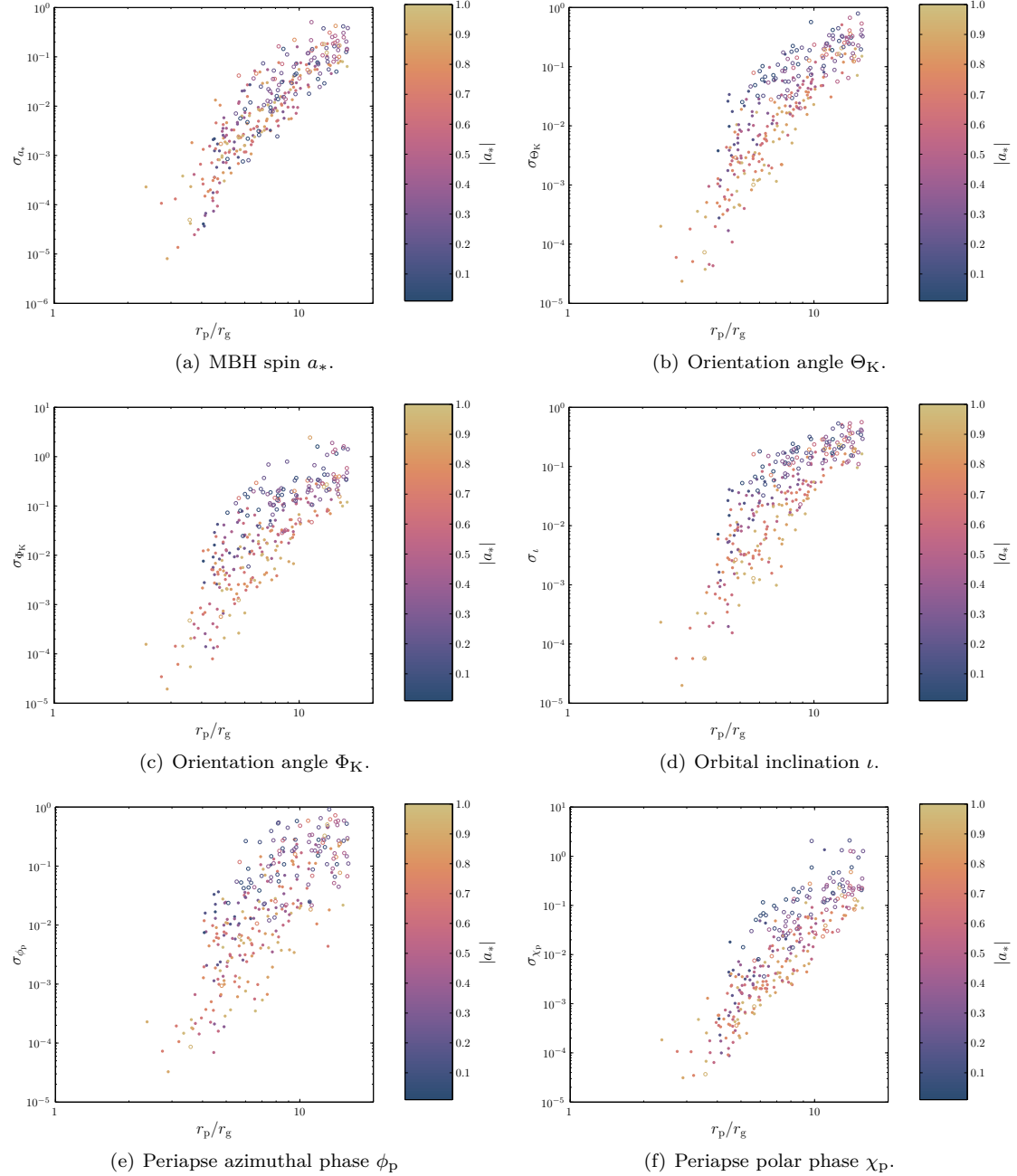


**Figure 15:** Parameter standard deviations versus periapsis  $r_p$ , showing dependence (or lack thereof) upon the spin magnitude  $|a_*|$ .

## 9 Extra-galactic sources

We have so far only been concerned with properties of bursts from our own galaxy. This is the best source for bursts because of its proximity. A natural continuation is to consider EMRBs from other MBHs. Rubbo *et al.* (2006) suggested that LISA should be able to detect EMRBs originating from the Virgo cluster, although the detectable rate might only be  $10^{-4}$  yr $^{-1}$  per galaxy (Hopman *et al.* 2007). We wish to investigate this possibility using our more accurate waveforms.

### 9.1 Detection with LISA

Space-based detectors are most sensitive from extreme-mass-ratio signals originating from MBHs with masses  $10^5$ – $10^6 M_\odot$ . Higher mass objects produce signals at too low frequencies. We considered several nearby MBHs that were likely candidates for detectable burst signals. Details are given in table 2. For each, we calculated SNRs at  $\sim 10^4$  different periapse distances following

Galaxy	$M_\bullet/10^6 M_\odot$	$R/\text{Mpc}$	References
Milky Way (MW)	4.31	0.00833	Gillessen <i>et al.</i> (2009)
M32 (NGC 221)	2.5	0.770	Verolme <i>et al.</i> (2002); Karachentsev <i>et al.</i> (2004)
Andromeda (M31, NGC 224)	140	0.770	Bender <i>et al.</i> (2005); Karachentsev <i>et al.</i> (2004)
Circinus	1.1	2.82	Graham (2008); Greenhill <i>et al.</i> (2003); Karachentsev <i>et al.</i> (2007)
NGC 4945	1.4	3.82	Greenhill <i>et al.</i> (1997); Karachentsev <i>et al.</i> (2007)
Sculptor (NGC 253)	10	3.5	Graham <i>et al.</i> (2011); Rodríguez-Rico <i>et al.</i> (2006); Rekola <i>et al.</i> (2005)
NGC 4395	0.36	4.0	Peterson <i>et al.</i> (2005); Thim <i>et al.</i> (2004)
NGC 3368	7.3	10.1	Graham <i>et al.</i> (2011); Nowak <i>et al.</i> (2010); Tonry <i>et al.</i> (2001)
NGC 3489	5.8	11.7	Graham <i>et al.</i> (2011); Nowak <i>et al.</i> (2010); Tonry <i>et al.</i> (2001)

**Table 2:** Sample of nearby MBHs that are candidates for producing detectable EMRBs.

the same method as in section 5.2.

The SNR depends upon many parameters. For a given MBH, the most important parameter is the periapse radius  $r_p$ . As shown in figure 7, there is a good correlation between  $\rho$  and  $r_p$ ; other parameters only produce scatter about this. The form of the  $\rho$ – $r_p$  relation depends upon the noise curve. To compare SNRs between MBHs, we parametrize the detectability in terms of a characteristic frequency

$$f_* = \sqrt{\frac{GM_\bullet}{r_p^3}}. \quad (77)$$

This allows comparison between different systems where the same periapse does not correspond to the same frequency, and thus the same point of the noise curve.

We also expect the SNR to scale with other quantities. We define a characteristic strain amplitude for a burst  $h_0$ ; we expect  $\rho \propto h_0$ , where the proportionality is set by a frequency-dependent function than includes the effect of the noise curve. Assuming that the strain is dominated by the quadrupole contribution, see equation (18),

$$h_0 \sim \frac{G}{c^6} \frac{\mu}{R} \frac{d^2}{dt^2} (r^2), \quad (78)$$

where  $r$  is a proxy for the position of the orbiting object. The characteristic rate of change is set by  $f_*$  and the characteristic length scale is set by  $r_p$ . Hence

$$h_0 \sim \frac{G}{c^6} \frac{\mu}{R} f_*^2 r_p^2 \quad (79)$$

$$\sim \frac{G^{5/2}}{c^6} \frac{\mu}{R} f_*^{-2/3} M_\bullet^{2/3}. \quad (80)$$

Using this, we can factor out the most important dependencies to give a scaled SNR

$$\rho_* = \left( \frac{\mu}{M_\odot} \right)^{-1} \left( \frac{R}{\text{Mpc}} \right) \left( \frac{M_\bullet}{10^6 M_\odot} \right)^{-2/3} \rho. \quad (81)$$

The scaled SNRs are plotted in figure 16. The plotted points are the average values of  $\ln \rho_*$  calculated for each periapse distance. The curve shows that EMRB SNR does scale as expected,

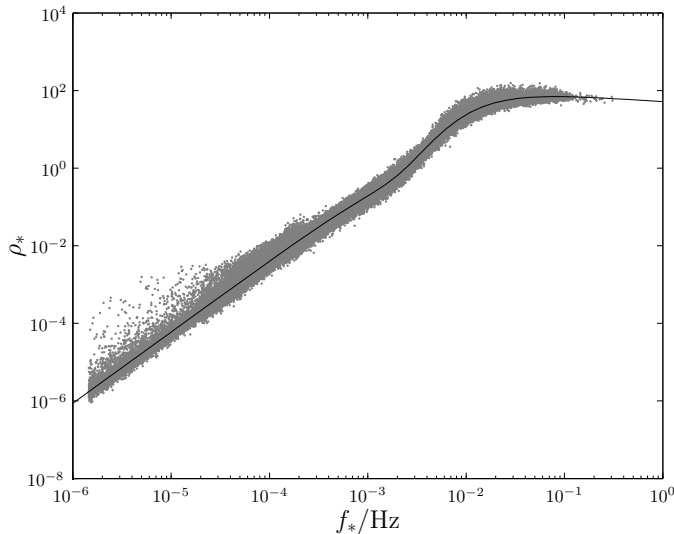


**Figure 16:** Scaled signal-to-noise ratio for EMRBs as a function of characteristic frequency.

and  $\rho_*$  can be described as a one-parameter curve. There remains some scatter about this (removing the averaging over intrinsic parameters increases this to about an order of magnitude); however, it is good enough for rough calculations.

We approximate the trend with a best-fit curve

$$\rho_* = \alpha_1 f_*^{\beta_1} \left[ 1 + (\alpha_2 f_*)^{\beta_2} \right] \left[ 1 + (\alpha_3 f_*)^{\beta_3} \right]^{-\beta_4}. \quad (82)$$

To fit this, we treat the problem as if it were a likelihood maximisation, with each averaged point having a Gaussian likelihood with standard deviation defined from the scatter because of the variation in the intrinsic parameters. The optimised values for LISA are

$$\begin{aligned} \alpha_1 &\simeq 8.93 \times 10^4; & \alpha_2 &\simeq 4.68 \times 10^2; & \alpha_3 &\simeq 1.84 \times 10^2; \\ \beta_1 &\simeq 1.84; & \beta_2 &\simeq 3.23; & \beta_3 &\simeq 1.27; & \beta_4 &\simeq 4.13. \end{aligned} \quad (83)$$

Using our fitted trends it is possible to invert equation (81) to find the furthest distance that bursts from an MBH of a given mass are detectable. In calculating the maximum SNR it is necessary to decide upon a minimum periapse radius. For the optimal case with a maximally rotating MBH, the innermost periapsis is  $r_p = r_g$ . For a non-rotating MBH, the innermost periapsis would be  $r_p = 4r_g$ . Figure 17 shows the detectability limit for  $\mu = 1M_\odot$  and  $\mu = 10M_\odot$

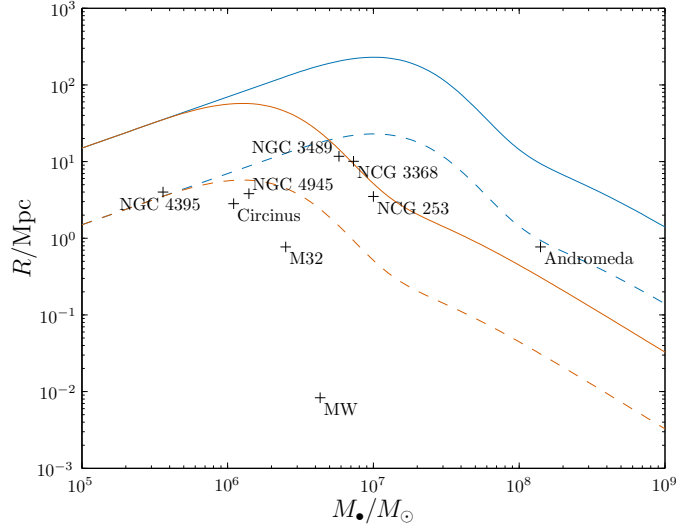


**Figure 17:** Limit of detection for EMRBs originating from MBHs of mass  $M_\bullet$  and distance  $R$  with CO of mass  $\mu = 1M_\odot$  (dashed line) or  $\mu = 10M_\odot$  (solid line). The detection threshold is assumed to be  $\rho = 10$ . The orange line is the limit for non-rotating MBHs, the blue line is for maximally rotating MBHs. Sources below the relevant line are potentially detectable. The trends should not be extrapolated to lower MBH masses.

COs. The more massive COs are detectable to a greater distance, but are also the more likely sources since mass segregation ensures they are more likely to be on orbits that pass close to the MBH. Limits using periapsis of  $r_g$  and  $4r_g$  are shown: intermediate spin values would have limits between these two. In any case, these are strict bounds; it is unlikely that we would observe a burst from the optimal orbit. Therefore bursts from MBHs outside the curve are impossible to detect and those inside may be possible, but need not be probable, to detect.

It appears that there are potentially many galaxies which could produce observable bursts. From our sample, all could be potentially detected. Andromeda could only be detected if it had a high spin value. It is therefore less promising than the others. NGC 3489, NGC 3368 and NGC 253 lie on the boundary of detectability for non-spinning sources with a  $10M_\odot$  CO. They are therefore of marginal interest: we do not necessarily need any special requirement for the spin, but such close orbits would be infrequent. NGC 4395, NGC 4945 and Circinus are around the boundary of detectability for a  $1M_\odot$  CO. Hence we could potentially see bursts from white dwarfs as well as BHs. M32 is the best extragalactic source, lying safely within the detection limit for  $1M_\odot$  COs.

Examining M32 in detail, the trend between the periapse radius and SNR is shown in figure 18. The fit is again for orbits with  $f_* < 1 \times 10^{-3}$  Hz to avoid the bucket of the noise curve. Bursts for a  $1M_\odot$  ( $10M_\odot$ ) can be detected with  $\rho > 10$  if the periapse is smaller than  $7r_g$  ( $14r_g$ ). We see that the general behaviour is the same as for the GC, but there are differences because of the position.

## 9.2 Detection with eLISA

We can repeat the analysis for eLISA. The scaled SNRs are shown in figure 19. Since Andromeda was only marginally of interest for the classic LISA design, we did not include it this time. The curve is fitted with

$$\begin{aligned} \alpha_1 &\simeq 7.39 \times 10; & \alpha_2 &\simeq 4.99 \times 10^3; & \alpha_3 &\simeq 5.27 \times 10; \\ \beta_1 &\simeq 1.47; & \beta_2 &\simeq 0.85; & \beta_3 &\simeq 1.76; & \beta_4 &\simeq 1.25. \end{aligned} \quad (84)$$

Using this to find the detectability range results in the curves shown in figure 20. The maximum

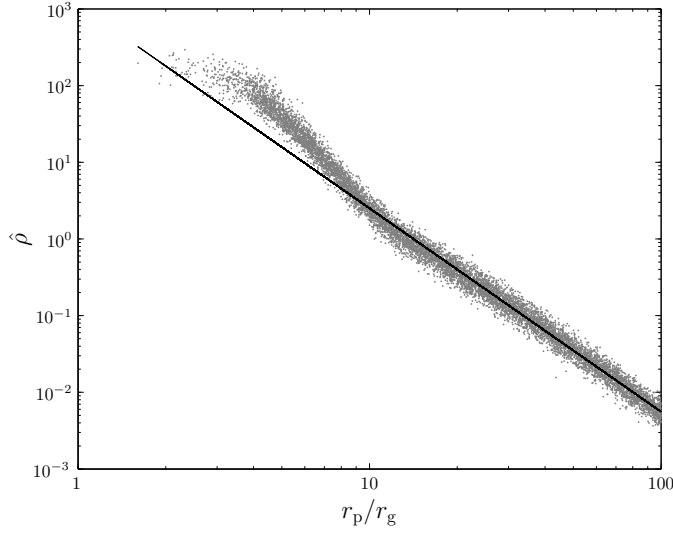


**Figure 18:** Signal-to-noise ratio as a function of periape radius for a  $\mu = 1M_{\odot}$  CO about the MBH of M32. The plotted points are the values obtained by averaging over each set of intrinsic parameters. The best fit line is  $\log(\hat{\rho}) = -2.65 \log(r_p/r_g) + 3.05$ . This is fitted to orbits with  $r_p > 18.8r_g$  and has a reduced chi-squared value of  $\chi^2/\nu = 1.26$ .

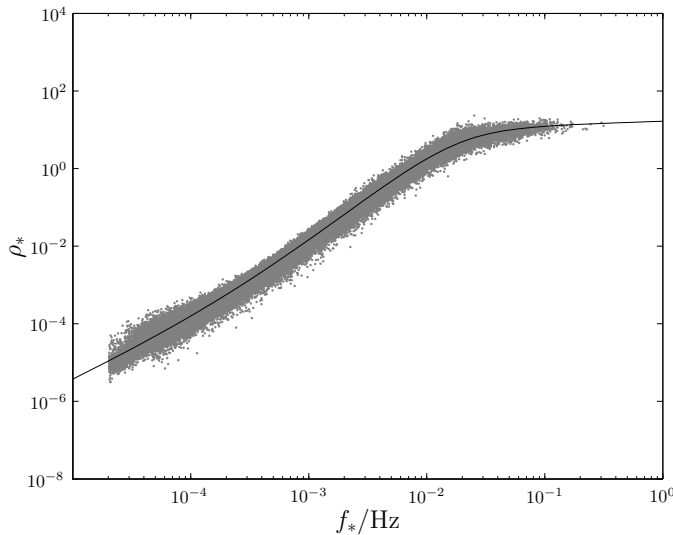


**Figure 19:** Scaled signal-to-noise ratio for EMRBs as a function of characteristic frequency for the eLISA design.

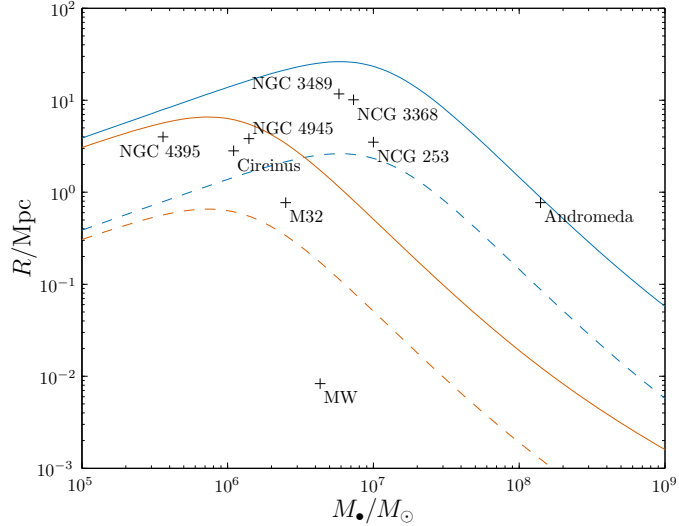


**Figure 20:** Limit of detection using eLISA for EMRBs originating from MBHs of mass  $M_\bullet$  and distance  $R$  with CO of mass  $\mu = 1M_\odot$  (dashed line) or  $\mu = 10M_\odot$  (solid line). The detection threshold is assumed to be  $\rho = 10$ . The orange line is the limit for non-rotating MBHs, the blue line is for maximally rotating MBHs. Sources below the relevant line are potentially detectable. The trends should not be extrapolated to lower MBH masses.

distances are reduced compared to the LISA case indicating that detectable bursts would be much rarer. There still remain a number of potential candidate galaxies. From our sample, Andromeda is on the very edge of possibility. NGC 3489, NGC 3368 and NGC 253 require a high spin, making them unlikely sources. Of the extragalactic sources, only M32 remains detectable with a  $1M_\odot$ , and still it requires a non-zero spin.

Using either noise curve we see that EMRBs could potentially be seen from a range of galaxies. The Galaxy's MBH remains securely detectable in either case. M32 is the next best. MBHs with masses  $\sim 10^6\text{--}10^7 M_\odot$  are observable to the greatest distance. We currently know of few MBHs with masses at the lower end of the spectrum,  $10^5\text{--}10^6 M_\odot$ , but these would be good potential candidates.

## 10 Discussion

We have outlined an approximate method of generating gravitational waveforms for EMRBs. This assumes that the orbits are parabolic and employs a numerical kludge approximation. The two coordinate schemes for a NK presented here yield almost indistinguishable results. We conclude that either is a valid choice for this purpose. There may be differences when the spin is large and the periapse is small:  $\sim 10\%$  for  $r_p \simeq 4r_g$ ,  $\sim 20\%$  for  $r_p \simeq 2r_g$ .

The waveforms created appear to be consistent with results obtained using Peters and Mathews waveforms for large periapses, indicating that they have the correct weak-field form. The NK approach should be superior to that of Peters and Mathews in the strong-field regime as it uses the exact geodesics of the Kerr spacetime. Comparisons with energy fluxes from black hole perturbation theory indicate that typical waveform accuracy may be of order 5%, but this is worse for orbits with small periapses, and may be  $\sim 20\%$ . These errors are greater than the differences resulting from the use of the alternative coordinate systems.

The signal-to-noise ratio of bursts is well correlated with the periapsis. For bursts from the GC the SNR (per unit mass) may be reasonably described as having a power-law dependence of

$$\log(\hat{\rho}) \simeq -2.7 \log\left(\frac{r_p}{r_g}\right) + 4.9, \quad (85)$$

except for the closest orbits ( $r_p \lesssim 7r_g$ ). Signals should be detectable for a  $1M_\odot$  ( $10M_\odot$ ) object if the periapse is  $r_p < 27r_g$  ( $r_p < 65r_g$ ), corresponding to a physical scale of  $1.7 \times 10^{11}$  m ( $4.1 \times 10^{11}$  m) or  $5.6 \times 10^{-6}$  pc ( $1.3 \times 10^{-5}$  pc).

We used MCMC results as a robust measure of parameter estimation accuracy. Potentially, it is possible to determine very precisely the key parameters defining the Galaxy's MBH's mass and spin, if the periapsis is sufficiently small. From our investigation it appears that we can achieve good results from a single EMRB with periapsis of  $r_p \simeq 10r_g$  for a  $10M_\odot$  CO. This translates to a distance of  $6 \times 10^{10}$  m or  $2 \times 10^{-6}$  pc. Orbits closer than this would be even better, and place stricter constraints. The best orbits yield uncertainties of almost one part in  $10^5$  for the MBH mass and spin, far exceeding existing techniques. Conversely, orbits with  $r_p \gtrsim 20r_g$  are unlikely to provide any useful information.

While we have only considered bursts from our own galaxy in detail, it should be possible to observe bursts from other nearby galaxies if their MBH is of the appropriate mass. The SNR of EMRBs obeys a number of scaling relations that allow us to check whether an MBH could produce detectable bursts. M32 is the best extragalactic candidate. However, even in this case, the of parameter space that can produce detectable bursts is small. The SNR shows a similar dependence upon periapsis as for the GC, and may be described by a power-law of

$$\log(\hat{\rho}) \simeq -2.7 \log\left(\frac{r_p}{r_g}\right) + 3.1, \quad (86)$$

for orbits with  $r_p \gtrsim 10r_g$ . For a  $1M_\odot$  ( $10M_\odot$ ) object, bursts should be detectable for periapses  $r_p \lesssim 7r_g$  ( $r_p \lesssim 14r_g$ ), corresponding to  $2.6 \times 10^{10}$  m ( $4.9 \times 10^{10}$  m) or  $8.4 \times 10^{-7}$  pc ( $1.6 \times 10^{-6}$  pc). This leads us to conclude that extragalactic bursts are likely to be rare.

## References

- Alexander, T. & Hopman, C.; *The Astrophysical Journal*; **697**(2):1861–1869; 2009.
- Amaro-Seoane, P., Aoudia, S., Babak, S. et al.; *Classical and Quantum Gravity*; **29**(12):124016(20); 2012.
- Amaro-Seoane, P., Gair, J.R., Freitag, M. et al.; *Classical and Quantum Gravity*; **24**(17):R113–R169; 2007.
- Andrieu, C. & Thoms, J.; *Statistics and Computing*; **18**(4):343–373; 2008.
- Antonucci, F., Armano, M., Audley, H. et al.; *Classical and Quantum Gravity*; **29**(12):124014(10); 2012.
- Anza, S., Armano, M., Balaguer, E. et al.; *Classical and Quantum Gravity*; **22**(10):S125–S138; 2005.
- Babak, S., Fang, H., Gair, J., Glampedakis, K. & Hughes, S.; *Physical Review D*; **75**(2):024005(25); 2007.
- Backer, D.C. & Sramek, R.A.; *The Astrophysical Journal*; **524**(2):805–815; 1999.
- Bahcall, J.N. & Wolf, R.A.; *The Astrophysical Journal*; **216**(3):883—907; 1977.
- Barack, L.; *Classical and Quantum Gravity*; **26**(21):213001(56); 2009.
- Barack, L. & Cutler, C.; *Physical Review D*; **69**(8):082005(24); 2004.
- Bédard, M.; *The Annals of Applied Probability*; **17**(4):1222–1244; 2007.
- Bédard, M.; *Journal of Computational and Graphical Statistics*; **17**(2):312–332; 2008a.
- Bédard, M.; *Stochastic Processes and their Applications*; **118**(12):2198–2222; 2008b.
- Bekenstein, J.D.; *The Astrophysical Journal*; **183**(2):657–664; 1973.
- Bélanger, G., Terrier, R., de Jager, O.C., Goldwurm, A. & Melia, F.; *Journal of Physics: Conference Series*; **54**(1):420–426; 2006.
- Bender, P., Brillet, A., Ciufolini, I. et al.; ‘LISA Pre-Phase A Report’; Technical report; Max-Planck-Institut für Quantenoptik; Garching; 1998.
- Bender, R., Kormendy, J., Bower, G. et al.; *The Astrophysical Journal*; **631**(1):280–300; 2005.
- Berti, E., Cardoso, V., Gonzalez, J.A. et al.; *Physical Review D*; **76**(6):064034(40); 2007.
- Berti, E. & Volonteri, M.; *The Astrophysical Journal*; **684**(2):822–828; 2008.
- Boyer, R.H. & Lindquist, R.W.; *Journal of Mathematical Physics*; **8**(2):265–281; 1967.
- Brenneman, L.W., Reynolds, C.S., Nowak, M.A. et al.; *The Astrophysical Journal*; **736**(2):103(10); 2011.
- Brenneman, L.W. & Reynolds, C.S.; *The Astrophysical Journal*; **652**(2):1028–1043; 2006.
- Carter, B.; *Physical Review Letters*; **26**(6):331–333; 1971.
- Carter, B.; *Physical Review*; **174**(5):1559–1571; 1968.
- Chandrasekhar, S.; *The Mathematical Theory of Black Holes*; Oxford Classic Texts in the Physical Sciences; Oxford: Oxford University Press; 1998.
- Cutler, C.; *Physical Review D*; **57**(12):7089–7102; 1998.
- Cutler, C. & Flanagan, E.E.; *Physical Review D*; **49**(6):2658–2697; 1994.
- Danzmann, K. & Rüdiger, A.; *Classical and Quantum Gravity*; **20**(10):S1–S9; 2003.
- de Felice, F.; *Journal of Physics A: Mathematical and General*; **13**(5):1701–1708; 1980.
- de la Calle Pérez, I., Longinotti, A.L., Guainazzi, M. et al.; *Astronomy and Astrophysics*; **524**:A50(22); 2010.
- Doeleman, S.S., Weintroub, J., Rogers, A.E.E. et al.; *Nature*; **455**(7209):78–80; 2008.
- Drasco, S. & Hughes, S.; *Physical Review D*; **69**(4):044015(11); 2004.
- Emmanoulopoulos, D., Papadakis, I.E., McHardy, I.M. et al.; *Monthly Notices of the Royal Astronomical Society*; **415**(2):1895–1906; 2011.
- Ferrarese, L. & Merritt, D.; *The Astrophysical Journal*; **539**(1):L9–L12; 2000.
- Finn, L.S.; *Physical Review D*; **46**(12):5236–5249; 1992.
- Gair, J.R., Kennefick, D.J. & Larson, S.L.; *Physical Review D*; **72**(8):084009(20); 2005.
- Gallo, L.C., Miniutti, G., Miller, J.M. et al.; *Monthly Notices of the Royal Astronomical Society*; **411**(1):607–619; 2011.
- Gammie, C.F., Shapiro, S.L. & McKinney, J.C.; *The Astrophysical Journal*; **602**(1):312–319; 2004.
- Gebhardt, K., Bender, R., Bower, G. et al.; *The Astrophysical Journal*; **539**(1):L13–L16; 2000.
- Gelman, A., Roberts, G.O. & Gilks, W.R.; in J.M. Bernardo, J.O. Berger, A.P. Dawid & A.F.M. Smith (eds.), *Bayesian Statistics*; Oxford Science Publications; 599–607; Oxford: Clarendon Press; 1996.
- Genzel, R., Schödel, R., Ott, T. et al.; *Nature*; **425**(6961):934–937; 2003.
- Ghez, A.M., Salim, S., Weinberg, N.N. et al.; *The Astrophysical Journal*; **689**(2):1044–1062; 2008.
- Gillessen, S., Eisenhauer, F., Trippe, S. et al.; *The Astrophysical Journal*; **692**(2):1075–1109; 2009.
- Glampedakis, K.; *Classical and Quantum Gravity*; **22**(15):S605–S659; 2005.
- Glampedakis, K., Hughes, S. & Kennefick, D.; *Physical Review D*; **66**(6):064005(12); 2002.
- Glampedakis, K. & Kennefick, D.; *Physical Review D*; **66**(4):044002(33); 2002.
- González, J.A., Sperhake, U., Brügmann, B., Hannam, M. & Husa, S.; *Physical Review Letters*; **98**(9):091101(4); 2007.
- Gradshteyn, I.S. & Ryzhik, I.M.; *Table of Integrals, Series, and Products*; London: Academic Press; sixth edition; 2000.
- Graham, A.W.; *Monthly Notices of the Royal Astronomical Society*; **379**(2):711–722; 2007.
- Graham, A.W.; *Publications of the Astronomical Society of Australia*; **25**(4):167; 2008.
- Graham, A.W., Erwin, P., Caon, N. & Trujillo, I.; *The Astrophysical Journal*; **563**(1):L11–L14; 2001.
- Graham, A.W., Onken, C.A., Athanassoula, E. & Combes, F.; *Monthly Notices of the Royal Astronomical Society*; **412**(4):2211–2228; 2011.
- Greenhill, L.J., Booth, R.S., Ellingsen, S.P. et al.; *The Astrophysical Journal*; **590**(1):162–173; 2003.
- Greenhill, L.J., Moran, J.M. & Herrnstein, J.R.; *The Astrophysical Journal*; **481**(1):L23–L26; 1997.

- Haario, H., Saksman, E. & Tamminen, J.; *Computational Statistics*; **14**(3):375; 1999.
- Haario, H., Saksman, E. & Tamminen, J.; *Bernoulli*; **7**(2):223–242; 2001.
- Haiman, Z. & Quataert, E.; in A.J. Barger (ed.), *Supermassive Black Holes in the Distant universe*; Astrophysics and Space Science Library; chapter 5, 147–186; Dordrecht: Kluwer Academic Publishers; 2004.
- Hamaus, N., Paumard, T., Müller, T. et al.; *The Astrophysical Journal*; **692**(1):902–916; 2009.
- Häring, N. & Rix, H.W.; *The Astrophysical Journal*; **604**(2):L89–L92; 2004.
- Harris, F.; *Proceedings of the IEEE*; **66**(1):51–83; 1978.
- Hastings, W.K.; *Biometrika*; **57**(1):97–109; 1970.
- Hawking, S.W.; *Communications in Mathematical Physics*; **25**(2):152–166; 1972.
- Hobson, M.P., Efstathiou, G. & Lasenby, A.; *General Relativity: An Introduction for Physicists*; Cambridge: Cambridge University Press; 2006.
- Hopman, C., Freitag, M. & Larson, S.L.; *Monthly Notices of the Royal Astronomical Society*; **378**(1):129–136; 2007.
- Huerta, E.A. & Gair, J.R.; *Physical Review D*; **79**(8):84021(22); 2009.
- Hughes, S.A. & Blandford, R.D.; *The Astrophysical Journal*; **585**(2):L101–L104; 2003.
- Israel, W.; *Physical Review*; **164**(5):1776–1779; 1967.
- Israel, W.; *Communications in Mathematical Physics*; **8**(3):245–260; 1968.
- Jahnke, K. & Macciò, A.V.; *The Astrophysical Journal*; **734**(2):92; 2011.
- Jaynes, E.T.; *Probability Theory: The Logic of Science*; Cambridge: Cambridge University Press; 2003.
- Jenrich, O., Binetruy, P., Colpi, M. et al.; ‘NGO Revealing a hidden Universe: opening a new chapter of discovery’; Technical report; European Space Agency; 2011.
- Karachentsev, I.D., Karachentseva, V.E., Huchtmeier, W.K. & Makarov, D.I.; *The Astronomical Journal*; **127**(4):2031–2068; 2004.
- Karachentsev, I.D., Tully, R.B., Dolphin, A. et al.; *The Astronomical Journal*; **133**(2):504–517; 2007.
- Kato, Y., Miyoshi, M., Takahashi, R., Negoro, H. & Matsumoto, R.; *Monthly Notices of the Royal Astronomical Society: Letters*; **403**(1):L74–L78; 2010.
- Kerr, R.; *Physical Review Letters*; **11**(5):237–238; 1963.
- King, A.R. & Pringle, J.E.; *Monthly Notices of the Royal Astronomical Society: Letters*; **373**(1):L90–L92; 2006.
- King, A.R., Pringle, J.E. & Hofmann, J.A.; *Monthly Notices of the Royal Astronomical Society*; **385**(3):1621–1627; 2008.
- Kormendy, J. & Richstone, D.; *Annual Review of Astronomy and Astrophysics*; **33**(1):581–624; 1995.
- Larson, S.L., Hellings, R.W. & Hiscock, W.A.; *Physical Review D*; **66**(6):062001(7); 2002.
- Larson, S.L., Hiscock, W.A. & Hellings, R.W.; *Physical Review D*; **62**(6):062001(10); 2000.
- Lohfink, A.M., Reynolds, C.S., Miller, J.M. et al.; *The Astrophysical Journal*; **758**(1):67; 2012.
- Lynden-Bell, D. & Rees, M.J.; *Monthly Notices of the Royal Astronomical Society*; **152**(4):461–475; 1971.
- MacKay, D.J.C.; *Information Theory, Inference and Learning Algorithms*; Cambridge: Cambridge University Press; 2003.
- Magorrian, J., Tremaine, S., Richstone, D. et al.; *The Astronomical Journal*; **115**(6):2285–2305; 1998.
- Malbon, R.K., Baugh, C.M., Frenk, C.S. & Lacey, C.G.; *Monthly Notices of the Royal Astronomical Society*; **382**(4):1394–1414; 2007.
- Marconi, A. & Hunt, L.K.; *The Astrophysical Journal*; **589**(1):L21–L24; 2003.
- Martel, K.; *Physical Review D*; **69**(4):044025(20); 2004.
- McClintock, J.E., Narayan, R., Davis, S.W. et al.; *Classical and Quantum Gravity*; **28**(11):114009(17); 2011.
- Merritt, D., Alexander, T., Mikkola, S. & Will, C.M.; *Physical Review D*; **81**(6):062002(17); 2010.
- Metropolis, N., Rosenbluth, A.W., Rosenbluth, M.N., Teller, A.H. & Teller, E.; *The Journal of Chemical Physics*; **21**(6):1087; 1953.
- Miller, J.M.; *Annual Review of Astronomy and Astrophysics*; **45**(1):441–479; 2007.
- Miniutti, G., Panessa, F., De Rosa, A. et al.; *Monthly Notices of the Royal Astronomical Society*; **398**(1):255–262; 2009.
- Misner, C.W., Thorne, K.S. & Wheeler, J.A.; *Gravitation*; New York: W. H. Freeman; 1973.
- Nardini, E., Fabian, A.C., Reis, R.C. & Walton, D.J.; *Monthly Notices of the Royal Astronomical Society*; **410**(2):1251–1261; 2011.
- Nowak, N., Thomas, J., Erwin, P. et al.; *Monthly Notices of the Royal Astronomical Society*; **403**(2):646–672; 2010.
- Nuttall, A.; *IEEE Transactions on Acoustics, Speech and Signal Processing*; **29**(1):84–91; 1981.
- Patrick, A.R., Reeves, J.N., Lobban, A.P., Porquet, D. & Markowitz, A.G.; *Monthly Notices of the Royal Astronomical Society*; **416**(4):2725–2747; 2011a.
- Patrick, A.R., Reeves, J.N., Porquet, D. et al.; *Monthly Notices of the Royal Astronomical Society*; **411**(4):2353–2370; 2011b.
- Peng, C.Y.; *The Astrophysical Journal*; **671**(2):1098–1107; 2007.
- Peters, P.C.; *Physical Review*; **136**(4B):B1224–B1232; 1964.
- Peters, P.C. & Mathews, J.; *Physical Review*; **131**(1):435–440; 1963.
- Peterson, B.M., Bentz, M.C., Desroches, L. et al.; *The Astrophysical Journal*; **632**(2):799–808; 2005.
- Press, W.; *Physical Review D*; **15**(4):965–968; 1977.
- Psaltis, D.; *Living Reviews in Relativity*; **11**(9); 2008.
- Rees, M.J.; *Annual Review of Astronomy and Astrophysics*; **22**(1):471–506; 1984.

- Reid, M.J., Readhead, A.C.S., Vermeulen, R.C. & Treuhaft, R.N.; *The Astrophysical Journal*; **524**(2):816–823; 1999.
- Reid, M.J., Menten, K.M., Genzel, R. et al.; *Astronomische Nachrichten*; **324**(S1):505–511; 2003.
- Rekola, R., Richer, M.G., McCall, M.L. et al.; *Monthly Notices of the Royal Astronomical Society*; **361**(1):330–336; 2005.
- Roberts, G.O., Gelman, A. & Gilks, W.R.; *The Annals of Applied Probability*; **7**(1):110–120; 1997.
- Roberts, G.O. & Rosenthal, J.S.; *Statistical Science*; **16**(4):351–367; 2001.
- Roberts, G.O. & Rosenthal, J.S.; *Journal of Applied Probability*; **44**(2):458–475; 2007.
- Robinson, D.C.; *Physical Review Letters*; **34**(14):905–906; 1975.
- Rodríguez-Rico, C.A., Goss, W.M., Zhao, J.H., Gomez, Y. & Anantharamaiah, K.R.; *The Astrophysical Journal*; **644**(2):914–923; 2006.
- Rosquist, K., Bylund, T. & Samuelsson, L.; *International Journal of Modern Physics D*; **18**(03):429–434; 2009.
- Rubbo, L.J., Holley-Bockelmann, K. & Finn, L.S.; *The Astrophysical Journal*; **649**(1):L25–L28; 2006.
- Ruffini, R. & Sasaki, M.; *Progress of Theoretical Physics*; **66**(5):1627–1638; 1981.
- Sathyaprakash, B. & Schutz, B.F.; *Living Reviews in Relativity*; **12**(2); 2009.
- Schmoll, S., Miller, J.M., Volonteri, M. et al.; *The Astrophysical Journal*; **703**(2):2171–2176; 2009.
- Sikora, M., Stawarz, Ł. & Lasota, J.; *The Astrophysical Journal*; **658**(2):815–828; 2007.
- Soltan, A.; *Monthly Notices of the Royal Astronomical Society*; **200**(1):115–122; 1982.
- Tanaka, T., Shibata, M., Sasaki, M., Tagoshi, H. & Nakamura, T.; *Progress of Theoretical Physics*; **90**(1):65–83; 1993.
- Thim, F., Hoessel, J.G., Saha, A. et al.; *The Astronomical Journal*; **127**(4):2322–2343; 2004.
- Thorne, K.S.; *The Astrophysical Journal*; **191**(2):507–519; 1974.
- Tonry, J.L., Dressler, A., Blakeslee, J.P. et al.; *The Astrophysical Journal*; **546**(2):681–693; 2001.
- Tremaine, S., Gebhardt, K., Bender, R. et al.; *The Astrophysical Journal*; **574**(2):740–753; 2002.
- Trippe, S., Paumard, T., Ott, T. et al.; *Monthly Notices of the Royal Astronomical Society*; **375**(3):764–772; 2007.
- Turner, M.; *The Astrophysical Journal*; **216**(2):610–619; 1977.
- Verolme, E.K., Cappellari, M., Copin, Y. et al.; *Monthly Notices of the Royal Astronomical Society*; **335**(3):517–525; 2002.
- Volonteri, M.; *The Astronomy and Astrophysics Review*; **18**(3):279–315; 2010.
- Volonteri, M., Madau, P., Quataert, E. & Rees, M.J.; *The Astrophysical Journal*; **620**(1):69–77; 2005.
- Volonteri, M. & Natarajan, P.; *Monthly Notices of the Royal Astronomical Society*; **400**(4):1911–1918; 2009.
- Volonteri, M., Sikora, M. & Lasota, J.P.; *The Astrophysical Journal*; **667**(2):704–713; 2007.
- Watson, G.N.; *A Treatise on the Theory of Bessel Functions*; Cambridge Mathematical Library; Cambridge: Cambridge University Press; second edition; 1995.
- Wilkins, D.; *Physical Review D*; **5**(4):814–822; 1972.
- Yu, Q. & Tremaine, S.; *Monthly Notices of the Royal Astronomical Society*; **335**(4):965–976; 2002.
- Yunes, N.N., Sopuerta, C.F., Rubbo, L.J. & Holley-Bockelmann, K.; *The Astrophysical Journal*; **675**(1):604–613; 2008.
- Yusef-Zadeh, F., Choate, D. & Cotton, W.; *The Astrophysical Journal*; **518**(1):L33–L35; 1999.
- Zoghbi, A., Fabian, A.C., Uttley, P. et al.; *Monthly Notices of the Royal Astronomical Society*; **401**(4):2419–2432; 2010.